J. Fluid Mech. (2024), *vol*. 1001, A36, doi:10.1017/jfm.2024.812

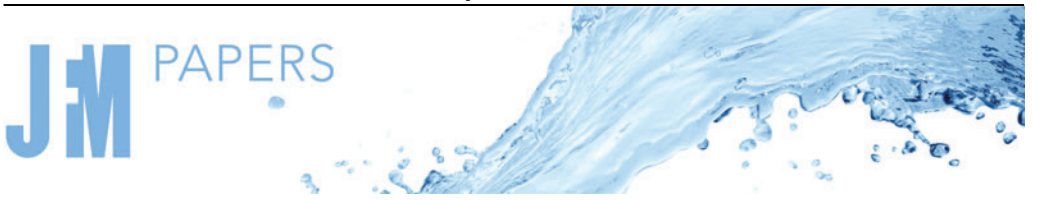

Flame acceleration and detonation transition in premixed and inhomogeneous supersonic flows

Wandong Zhao[1], **Ralf Deiterding**[2], **Xiaodong Cai**[1], **Jianhan Liang**[1,†], **Xiong Yang**[1] **and Mingbo Sun**[1,†]

[1]College of Aerospace Science and Engineering, National University of Defense Technology, Changsha 410073, PR China

[2]AMROC CFD, Brookweg 167, 26127 Oldenburg, Germany

(Received 1 November 2023; revised 19 April 2024; accepted 25 June 2024)

The reactive Navier–Stokes equations with adaptive mesh refinement and a detailed chemical reactive mechanism (11 species, 27 steps) were adopted to investigate a detonation engine considering the injection and supersonic mixing processes. Flame acceleration and deflagration-to-detonation transition (DDT) in a premixed/inhomogeneous supersonic hydrogen–air mixture with and without transverse jet obstacles were addressed. Results demonstrate the difficulty in undergoing DDT in the premixed/inhomogeneous supersonic mixture within a smooth chamber. By contrast, multiple transverse jets injected into the chamber aid detonation transition by introducing perturbed vortices, shock waves and a suitable blockage ratio. Increasing distance between the leading shock and the flame tip impedes detonation transition due to an insufficient blockage ratio. The extremely perturbed distributions of fuel-lean and fuel-rich mixtures lead to more complicated flame structures. Also, a larger flame thickness appears in the inhomogeneous mixture compared with the premixed mixture, resulting in a lower combustion temperature. The key findings are that the DDT, detonation quenching and reinitiation are generated in the inhomogeneous supersonic mixture, but both DDT mechanisms are ascribed to a strong Mach stem with the Zel'dovich gradient mechanism. Additionally, the obtained results demonstrate that an intensely fuel-lean mixture (equivalence ratio = 0.15) results in a partially decoupled flame front. However, detonation reinitiation and subsequent self-sustained detonation occur when a fierce shock wave propagates through a highly sensitive mixture, even within a smaller and elongated area. Moreover, the inhomogeneous mixture also augments the propagation speed and detonation cell structure instabilities and delays the sonic point resulting from the extending non-equilibrium reaction.

Key words: detonation waves, detonations, combustion

† Email addresses for correspondence: jhleon@vip.sina.com, sunmingbo@nudt.edu.cn

1. Introduction

Flame acceleration (FA) and deflagration-to-detonation transition (DDT) are common phenomena in industrial scenarios, such as in coal mines and fuel leakage in fuel storage or pipelines (Oran, Chamberlain & Pekalski 2020; Fan & Xiao 2022). However, FA and DDT can also be employed within a detonation-based engine with high thermal efficiency thanks to its approximate isovolumic combustion, such as a pulse detonation engine (PDE) and rotate detonation engine (RDE) (Roy *et al.* 2004). Consequently, there has been significant interest in recent decades in understanding the processes and mechanisms of FA and achieving rapid detonation transition.

A most robust and effective approach to obtain the onset of detonation is to utilize FA without a direct initiation that requires highly transient energy deposition. Flame acceleration would generate a detonation transition condition in the region of the deflagration flame and leading shock wave (LSW). Consequently, solid objects such as a wedge, orifice, ring or Shchelkin spiral are applied to stimulate FA. The effects of blockage ratio (*Br*) (Goodwin, Houim & Oran 2016), types of mixtures (Sun & Lu 2020), types of solid obstacles (Xiao & Oran 2020) and arrangements of the solid object (Gamezo, Ogawa & Oran 2007; Gamezo, Bachman & Oran 2021) on FA and DDT mechanisms were reported by many former studies. Concerning an air-breathing detonation engine, a large number of solid objects arranged within the combustion chamber would result in high pressure or propulsion loss (Cooper *et al.* 2002; Roy *et al.* 2004). Subsequently, transverse jet obstacles injected into the chamber have been introduced to shorten the DDT run-up time (T_{DDT}) and DDT run-up distance (L_{DDT}). After this idea was first proposed by Ahmed & Forliti (2009) and Knox *et al.* (2011), the effects of the components of jet obstacle, jet pressure and jet size (Frolov *et al.* 2017; McGarry & Ahmed 2017; Peng *et al.* 2018, 2019; Cheng *et al.* 2020, 2021*a*,*b*; Tarrant *et al.* 2020; Zhang *et al.* 2024) on FA and DDT were studied comprehensively in recent years. It was found that the transverse jet obstacle has a dramatic impact on the performance in regard to triggering the detonation transition as it introduces a lot of turbulence flows and vortices and also provides an appropriate *Br*.

Many brilliant studies related to FA and DDT have been investigated in detail using numerical and experimental means when employing transverse jet obstacles. Nevertheless, the mixtures in most of the above studies are considered stoichiometric and in a quiescent state. By contrast, most mixtures in real-world accidents are maldistributions with large temperature, pressure and concentration gradients. As such, to address more practical scenarios, the effects of the non-uniform mixture with horizontal or transverse concentration gradients or inert gas on FA (Vollmer, Ettner & Sattelmayer 2012; Boeck, Hasslberger & Sattelmayer 2014; Zheng *et al.* 2019; Saeid, Khadem & Emami 2021), DDT (Ishii & Kojima 2007; Vollmer *et al.* 2012; Ettner, Vollmer & Sattelmayer 2013; Zheng *et al.* 2019) and detonation propagation (Thomas, Sutton & Edwards 1991; Fang *et al.* 2017; Iwata, Nakaya & Tsue 2017; Mi *et al.* 2017; Han, Wang & Law 2019; Iwata *et al.* 2021; Yao *et al.* 2022) characteristics have been investigated through experimental and numerical tools.

Thomas *et al.* (1991) conducted prior research on the detonation behaviour in the concentration gradient mixture that was generated by a sliding valve to control the diffusion time in a vertical tube. They revealed that FA would be generated in a fuel concentration gradient, resulting in a second shock wave, and the onset of detonation is more likely to occur in the smooth concentration, whereas the DDT may fail in the steeper concentration mixture. In Oran, Jones & Sichel's (1992) study, a series of shock-detonation structures were revealed in the two layers formed by differently diluted hydrogen–oxygen mixtures and an inert gas when an overdriven detonation wave or Chapman–Jouguet (CJ)

detonation propagates into these layers. Kuznetsov *et al.* (1998) experimentally found that the sharpness of the concentration gradient mixture with variable width in a less reactive acceptor mixture has a dramatic influence on the detonation propagation and reported that a donation wave propagates in the downstream tube without decay in the smooth gradient, but it always decays in a steep gradient. Sochet, Lamy & Brossard (2000) presented experimental research on the detonability in a hemispherical mixture through the gaseous mixture diffusing to air due to molecular diffusion, gravity and turbulence. The limit time between the two explosion behaviours was proposed, and the limit time delay was studied according to the degree of the mixture concentration gradient by changing the mixture component and confining volume. A variation of detonation propagation cellular structure from a diamond to a parallelogram profile obtained by smoke foil was revealed in the inhomogeneous mixture in Ishii & Kojima's (2007) research. A calibrated one-step reaction model was employed to simulate the detonation propagation in low-activation and high-activation energy mixtures with a normal concentration gradient in Kessler, Gamezo & Oran's (2011, 2012) research. The fuel-lean and fuel-rich mixtures near the wall resulted in a complex detonation front structure. Ettner *et al.* (2013) numerically simulated the detonation front profile under the effect of a concentration gradient by using the Euler equation with eight species components, and they reported that, in a steep concentration, a Mach stem is formed and results in an asymmetric pressure load on the channel wall. Boeck *et al.* (2016) studied the detonation propagation in a mixture with a transverse concentration gradient. They suggested that single-head detonation wave propagation with an intense transverse wave is formed in the fuel-rich region, and a large amount of unburned mixture is generated. Meanwhile, Boulal, Vidal & Zitoun (2016) also experimentally studied the detonation quenching mechanism in an inhomogeneous mixture. The detonation quenching took place in the equivalence ratio (ER) distribution from a large lean to lean gradient, and they suggested that, with the inhomogeneous mixture, researchers should pay more attention to a detonation engine, especially the detonation dynamic that firstly quenches then the re-initiates it. In order to study the deficit of the flame propagation velocity and the flame front structure, Han *et al.* (2019) conducted a comprehensive study on the mechanisms of the detonation propagation in H_2–O_2 mixtures with linear transverse concentration gradients, and the cellular instability is increased in a high-concentration gradient, resulting in a more unburned H_2 pocket downstream and a deficit of the detonation velocity owing to the non-equilibrium chemical reaction.

Recently, a tulip flame propagation in the concentration gradient mixture was revealed in the Sun & Lu (2020) work. In Song, Han & Cao's (2020) research, the detonation propagation in an inhomogeneous mixture that has a sinusoidal distribution was studied by employing a high mesh resolution and a detailed chemical reaction mechanism. Multi-head and single-head modes were formed in the low-concentration and high-concentration gradients, respectively. Besides that, by employing the OpenFOAM CFD toolbox, Jiang *et al.* (2022*a*,*b*) also studied detonations that propagate into a 90-degree bifurcated channel with a transverse concentration gradient. The mechanisms of detonation diffraction, quenching and reinitiation were revealed.

Furthermore, the detonation propagation with inert gas has also received increasing attention. Mi *et al.* (2017) numerically conducted detonation propagation research in spatially inhomogeneous mixtures. The averaged propagation velocity was consistent with the theoretical CJ value when the non-uniformity was small, while it had a higher propagation velocity when there was enough of the inhomogeneous mixture. The detonation propagation in an inhomogeneous mixture with an inert layer was also

investigated in Wang *et al.*'s (2020) work, and they found that the detonation reinitiation and detonation failure depend on the spacing and thickness between the two inert layers. Metrow, Gray & Ciccarelli (2021) carried out experimental and numerical research on the detonation propagation in a mixture with inert gas. They reported that the detonation cellular size is just slightly larger than in the stoichiometric mixture. More recently, Tang-Yuk *et al.* (2022) presented one- and two-dimensional investigations of the detonation transmission as it passes through the inert gas. They revealed that the critical thickness of the inert gas in the successful detonation reinitiation is related to the Zel'dovich–von Neumann–Döring (ZND) induction length and effective activation energy.

On the other hand, FA and DDT processes under the influence of the concentration gradient mixture are also studied. Vollmer *et al.* (2012) researched the inhomogeneous mixture within a solid-laden combustion chamber. It was found that predicting DDT becomes more challenging in the inhomogeneous mixture than in the premixed mixture, and it depends on the configuration of the *Br* and the length scale of the chamber. Like Vollmer *et al.*'s (2012) study, Boeck *et al.* (2014) also experimentally studied FA and DDT in the hydrogen/air inhomogeneous mixture, by controlling the diffusion time. It was found that a higher flame surface area is formed in the non-uniform mixture compared with the premixed mixture in the smooth chamber.

In contrast, within the solid chamber, the concentration gradient can either enhance or diminish the FA. Wang & Wen (2017) numerically studied the FA and DDT in an inhomogeneous mixture using the set-up proposed by Ettner *et al.* (2013). They observed many unburned pockets behind the detonation wave, particularly in the areas with high hydrogen concentration. Azadboni *et al.*'s (2019) investigated the FA and DDT processes in both premixed and inhomogeneous mixtures, both experimentally and numerically. They obtained similar results, showing that transverse concentration gradients can either enhance or reduce FA.

Recently, Zheng *et al.* (2019) conducted a high mesh resolution simulation of the FA and DDT in non-uniform mixtures. They found that, in the inhomogeneous mixture, there is continuous mixing after the flame front that results in a larger flame surface area than that in the premixed mixture, but the local heat release rate is low. More recently, the FA and DDT mechanisms in the inhomogeneous mixture were numerically studied in chambers with different obstacle spacing through the OpenFOAM CFD toolbox (Saeid, Khadem & Emami 2021). It was found that the DDT is only formed in the inhomogeneous mixture in the 30 % *Br* chamber with a 15 % average concentration, and at the 30 % average concentration, the DDT takes place in both premixed and inhomogeneous mixtures. Further on, the effect of diffusion time on the FA and DDT in the non-uniform mixture was also investigated in Saeid *et al.*'s (2022) work, and they found three different regimes of the DDT mechanism in the fuel-rich non-uniform mixture.

Amid the works mentioned above, most mixtures can be considered as one-dimensional gradients in parallel or perpendicular directions. Nevertheless, a real-world mixture would have a more uneven distribution with more complicated temperature, pressure and ER gradients rather than an artificial distribution with a linear or sinusoidal relationship. The concentration mixture is usually set in a static state. However, in practical scenarios, the inhomogeneous mixture may have a high velocity before mixture ignition, especially in the PDE and RDE.

Consequently, the FA or detonation propagation in real-world scenarios may be complicated, and the onset of detonation may pose greater challenges (Zhao *et al.* 2023*a*). Most investigations related to the flame front structure focus on the time evolution during the detonation propagation stage. However, there is a noticeable lack of studies on the

DDT mechanism and flame propagation in the inhomogeneous supersonic mixture with perturbed concentration gradients. Therefore, studying the FA, DDT, detonation quenching and propagation is crucial when considering a more realistic detonation engine under ejection and mixing processes.

For these reasons, the motivation of the current investigation is to understand the effect of inhomogeneous supersonic mixtures with perturbed concentration gradients considering the ejection and mixing processes on the FA, DDT, detonation quenching and detonation propagation under a supersonic flow condition. The flame front structures during the FA period in the premixed and inhomogeneous mixtures are reported in detail. The successful and unsuccessful DDT mechanisms in inhomogeneous mixtures are also revealed comprehensively. Moreover, the key findings of the DDT, detonation quenching and detonation reinitiation evolution are revealed. The corresponding critical ER for detonation quenching and DDT mechanisms is also reported. Learning from the previous studies, multiple transverse jet obstacles, as discussed above, are employed to activate the DDT in the inhomogeneous supersonic mixture.

Of note, here, we focus solely on a single case involving an inhomogeneous supersonic mixture undergoing the mixing process with $Ma = 1.5$ (where Ma is the Mach number), derived from a practical air-breathing PDE with a new type of inlet valve. The unsteady, reactive and compressible Navier–Stokes (N-S) equations are employed to carry out the mixing, FA, DDT and detonation propagation in a two-dimensional (2-D) combustion chamber with a detailed chemistry reaction mechanism and a high mesh resolution deploying a structured adaptive mesh refinement (AMR) technique. The solver is based on the AMROC (AMR object-oriented C++), successfully applied to resolve FA and detonation propagation (Cai *et al.* 2017, 2018; Peng *et al.* 2018). The chemical reaction is modelled by an Arrhenius-type equation from a detailed chemical reaction mechanism with 11 species and 27 reactive steps proposed by Burke *et al.* (2012).

2. Physical and numerical models

2.1. *Computational configuration*

Schematic illustrations of the configuration and boundary conditions are provided in figure 1 for both the premixed and inhomogeneous mixtures, considering the fuel injection and mixing processes under supersonic flow conditions. Both configurations feature inlet isolation and combustion chamber sections. Two hot spots, located in the upper and lower walls between the connection parts, are employed to ignite the premixed and inhomogeneous mixtures after closing the inlet valve. This approach has been widely adopted in DDT simulations in former studies (Gamezo, Ogawa & Oran 2008; Goodwin *et al.* 2016; Peng *et al.* 2018; Xiao & Oran 2020; Gamezo *et al.* 2021). The premixed hydrogen–air mixture and incoming air with temperature $T = 281.7$ K and pressure $p = 0.09$ MPa are filled into the combustion chamber of configurations A and B, respectively. The detailed parameters of the initial premixed mixture are given in table 1. The theoretical parameters of the post-shock, CJ state and laminar flame properties for the currently premixed mixture are also illustrated in table 1, which are obtained from Cantera (Goodwin, Moffat & Speth 2009) using Burke *et al.*'s (2012) mechanism. Of note, the detonation cellular size is calculated by the empirical correlation model provided by Ng, Ju & Lee (2007) that considers the ZND reaction zone as well as the reaction structure.

Regarding configuration A, two cases without and with transverse jet obstacles are selected during the FA after the mixture ignition, corresponding to case 1 and case 2. Concerning configuration B, two groups of head-on transverse fuel jets are located in

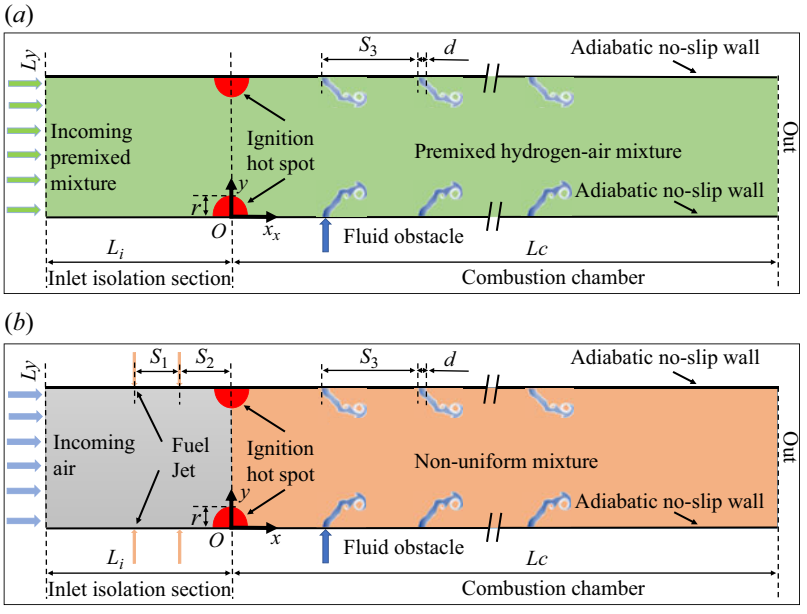

Figure 1. Schematic illustration of the combustion configuration and boundary conditions for an air-breathing PDE with (configuration A) premixed and (configuration B) inhomogeneous mixtures in a supersonic flight condition.

Quantity	Value	Definition
P_0	0.09 MPa	Initial pressure
T_0	281.7 K	Initial temperature
D_0	0.8035 kg m^{-3}	Initial density
M	20.91 g mol^{-1}	Molecular weight
P_{VN}	29.44 P_0	Pressure at von Neumann state
T_{VN}	5.41 T_0	Temperature at von Neumann state
D_{VN}	2.109 kg m^{-3}	Density at von Neumann state
S_1	≈2.136 m s^{-1}	Laminar flame speed
L_1	≈0.36 mm	Laminar flame thickness
P_{CJ}	16.56 P_0	Pressure at CJ point
T_{CJ}	10.48 T_0	Temperature at CJ point
D_{CJ}	1.5205 kg m^{-3}	Density at CJ point
V_{CJ}	1974.95 m s^{-1}	CJ detonation velocity
X_d	0.9–1.6 cm	Detonation cell width

Table 1. The thermodynamic properties of the premixed hydrogen–air mixture and the corresponding CJ parameters.

the isolation section when $t = 0.2$–1.04 ms. After the end of the mixing process, the hydrogen–air inhomogeneous mixture is formed in the combustion chamber under the supersonic incoming air. Similarly, as in configuration A, two cases without and with transverse jet obstacles are also considered during the FA, corresponding to case 3 and case 4. All parameters of the current cases are illustrated in table 2. Details of components for the incoming mixture, fuel jet and jet obstacle for different cases are listed in table 3.

Case	Mixture	Jet obstacles	Jet number	Jet pressure	Jet component
1	Premixed	no	—	—	—
2	Premixed	yes	4 groups	0.6 MPa, 1.2 MPa	Mixture
3	Inhomogeneous	No	—	—	—
4	Inhomogeneous	yes	4 groups	0.6 MPa, 1.2 MPa	Air

Table 2. The current cases employed for the FA and DDT.

Case	Incoming (H_2: O_2: N_2)	Fuel jet (H_2: O_2: N_2)	Jet obstacle (H_2: O_2: N_2)
1	2: 1: 3.76	—	—
2	2: 1: 3.76	—	2: 1: 3.76
3	0: 1: 3.76	2: 1: 3.76	—
4	0: 1: 3.76	2: 1: 3.76	0: 1: 3.76

Table 3. Parameters of component molar ratio of incoming air, fuel jet and transverse jet obstacles for the employed cases.

The domain sizes of the isolation section and combustion chamber are $L_i \times L_y = 180\ \text{mm} \times 20\ \text{mm}$ and $L_c \times L_y = 800\ \text{mm} \times 20\ \text{mm}$, respectively. The fuel jet pressure is 1.0 MPa. The width of the fuel jet is 0.2 mm. Four groups of head-on transverse jet obstacles are employed, which are adopted to introduce a host of turbulent flows and also provide a suitable Br by acting as solid objects, as reported by previous studies (Knox *et al.* 2011; Cheng *et al.* 2021*a*; Zhao *et al.* 2021). The pressure of the first and second groups of jet obstacles is $p = 0.6$ MPa and $p = 1.2$ MPa to accommodate the pressure gain combustion in the FA process. The transverse jet obstacles are successively injected into the combustion chamber after the mixture ignition. The operation times for the first, second, third and fourth head-on jets in case 4 are 1.1–1.3 ms, 1.15–1.4 ms, 1.3–1.5 ms and 1.4–1.6 ms, respectively. The width of all jet obstacles is $d = 2$ mm. The fuel jet exit gap is defined as S_1, and the distance between the centre of the hot spot and the nearest fuel jet is defined as S_2, as illustrated in figure 1(*b*). The values of S_1 and S_2 are set as $S_1 = 20$ mm and $S_2 = 30$ mm, respectively. The spacing interval between the jet obstacles is $S_3 = 90$ mm.

Concerning the boundary condition (BC), a supersonic velocity ($U = 504.76\ \text{m s}^{-1}$) inlet BC is first applied on the right side of the computational domain to simulate the mixing process. In the next process, after closing the inlet valve, the velocity inlet BC is changed to a no-slip and adiabatic wall owing to the air-breathing PDE operation during the FA and DDT processes. Furthermore, two hot spots with temperature $T = 2500$ K and slightly high-pressure $p = 0.5$ MPa are employed to ignite the premixed and inhomogeneous mixtures. The pressure inlet BC is utilized for all jets. A no-slip and adiabatic wall BC is adopted in the upper and lower walls of the computational domain. It is worth mentioning that the adiabatic wall BC may result in a slightly faster FA compared with the isothermal wall BC. The detailed results of the effect of the isothermal wall on the FA and DDT can be found in former literature (Han *et al.* 2020; Yhuel, Ribert & Domingo 2023). The current study focuses on the premixed and non-uniform mixtures; hence, we do not consider the isothermal wall's influence. Additionally, an outflow BC is specified on the right side of the computational domain.

2.2. *Governing equations and numerical methods*

The unsteady reactive 2-D N-S equations are employed to solve the multiple species flows, FA and DDT processes in the current study, and the governing equations are given as follows with a conservation flux vector (Cai *et al.* 2018):

$$\frac{\partial \boldsymbol{U}}{\partial t} + \frac{\partial (\boldsymbol{F}_x - \boldsymbol{G}_x)}{\partial x} + \frac{\partial (\boldsymbol{F}_y - \boldsymbol{G}_y)}{\partial y} = S_{chem}, \tag{2.1}$$

where $\boldsymbol{U}$ is the vector of the state parameter. Here, $\boldsymbol{F}_x$ and $\boldsymbol{F}_y$ denote the convection fluxes, and the quantity S_{chem} is the source term that is given by the mixture's chemical reaction (Zhao *et al.* 2023*b*). These vector-valued quantities are

$$\boldsymbol{U} = \begin{bmatrix} \rho_i \\ \rho u \\ \rho v \\ \rho E \end{bmatrix}, \quad \boldsymbol{F}_x = \begin{bmatrix} \rho_i u \\ \rho u^2 + p \\ \rho uv \\ u(\rho E + p) \end{bmatrix}, \quad \boldsymbol{F}_y = \begin{bmatrix} \rho_i v \\ \rho uv \\ \rho v^2 + p \\ v(\rho E + p) \end{bmatrix}, \quad S_{chem} = \begin{bmatrix} \dot{\boldsymbol{\omega}}_i \\ 0 \\ 0 \\ 0 \end{bmatrix}, \tag{2.2a–d}$$

in which u, v and e are the horizontal velocity, the normal velocity and total energy, respectively (Cai *et al.* 2018). Also, ρ in (2.2) denotes the component density and i equals 1, 2, 3 …, N_{sp}, with N_{sp} denoting the total number of species. The total energy E is given by

$$E = \sum_{n=1}^{N_{sp}} Y_i h_i - \frac{p}{\rho} + \frac{1}{2}(u^2 + v^2), \tag{2.3}$$

where h_i denotes the specific enthalpy of the species and p is obtained by a partial pressure equation for each species with perfect gas theory that reads

$$p = \sum_{n=1}^{N_{sp}} p_i = \sum_{n=1}^{N_{sp}} \rho Y_i R_i T, \quad \text{with } R_i = R/W_i, \tag{2.4}$$

in which R denotes the universal gas constant, W_i is the molar mass of the ith species and $\dot{\boldsymbol{\omega}}_i$ in (2.2) are the mass generation rates obtained from a specific chemical reaction mechanism J as

$$\dot{\boldsymbol{\omega}}_i = \sum_{j=1}^{J} (v_{ji}^r - v_{ji}^f) \left[k_j^f \prod_{n=1}^{N_{sp}} \left(\frac{\rho_n}{W_n} \right)^{v_{jn}^f} - k_j^r \prod_{n=1}^{N_{sp}} \left(\frac{\rho_n}{W_n} \right)^{v_{jn}^f} \right], \quad i = 1, \ldots, N_{sp}, \tag{2.5}$$

where v_{ji}^r and v_{ji}^f denote the stoichiometric coefficients of forward and reverse chemical reactions. The elementary chemical reaction with an Arrhenius equation was adopted to evaluate the reaction rates (Ivanov, Kiverin & Liberman 2011; Cai *et al.* 2018; Han *et al.* 2020) as

$$k_j^{f/r} = A_j^{f/r} T^{\beta_j^{f/r}} \exp\left(-\frac{E_j^{f/r}}{RT} \right). \tag{2.6}$$

The chemical kinetics package CHEMKIN is utilized to evaluate equations (2.5) and (2.6) in accordance with a specific chemical reactive mechanism. The quantities $\boldsymbol{G}_x$ and $\boldsymbol{G}_y$ in

(2.1) represent the diffusion fluxes (Cai *et al.* 2018)

$$\boldsymbol{G}_x = (\rho D_i(\partial Y_i/\partial x), \tau_{xx}, \tau_{xy}, u\tau_{xx} + v\tau_{xy} - q_x), \tag{2.7}$$

$$\boldsymbol{G}_y = (\rho D_i(\partial Y_i/\partial y), \tau_{yx}, \tau_{yy}, u\tau_{yx} + v\tau_{yy} - q_y). \tag{2.8}$$

The shear stress terms in (2.6) and (2.7) are further governed by

$$\tau_{xx} = \mu\left(\frac{4}{3}\frac{\partial u}{\partial x} - \frac{2}{3}\frac{\partial v}{\partial y}\right), \quad \tau_{yx} = \tau_{xy} = \mu\left(\frac{\partial v}{\partial x} + \frac{\partial u}{\partial y}\right), \quad \tau_{yy} = \mu\left(\frac{4}{3}\frac{\partial v}{\partial y} - \frac{2}{3}\frac{\partial u}{\partial x}\right), \tag{2.9a–c}$$

in which μ is the dynamic viscosity of the mixture. The heat fluxes in (2.7) and (2.8) are determined by

$$q_x = -k\partial T/\partial x - \rho\sum_{i=1}^{n} h_i D_i \partial Y_i/\partial x, \tag{2.10}$$

$$q_y = -k\partial T/\partial y - \rho\sum_{i=1}^{n} h_i D_i \partial Y_i/\partial y, \tag{2.11}$$

where k and D are the mixture-averaged thermal conductivity and mass diffusivities, respectively. The coefficients for the dynamic viscosity μ and the thermal conductivity k of the mixture are calculated by the formulas of Bird, Stewart & Lightfoot (2006) and Mathur, Tondon & Saxena (1967). The mass diffusion coefficients for an averaged molecular species are modelled by a simplified equation that is inversely proportional to the pressure. The transport variables, including viscosity, conductivity and diffusion, are calculated by the CHEMKIN-II package.

2.3. *Numerical methods and chemical reaction mechanism*

The governing equations mentioned above were solved in the open-source codes in the AMROC with the AMR approach. In terms of the numerical scheme, a hybrid Roe–HLL (Harten–Lax–van Leer) Riemann solver in AMROC was utilized to discretize the upwind fluxes to avoid some unphysical total density and internal energy near vacuum as a result of the Roe linearization (Deiterding 2003; Zhao *et al.* 2022*a*,*b*). By setting a refactor function, the MUSCL (monotone upwind scheme for conservation laws) scheme together with the Minmod limiter was employed for the reconstruction of the conservation flux vector. The central difference scheme was used to discretize the diffusion term in (2.1). Concerning the chemical reaction source, the Godunov splitting scheme with first-order accuracy was applied, which has enough accuracy compared with Strang splitting, as reported by Deiterding (2003). For the time discretization, a semi-implicit generalized Runge–Kutta scheme with fourth-order precision was adopted for the integration of the chemical kinetics (Kaps & Rentrop 1979), and a dynamic time step was assumed under a fixed Courant–Friedrichs–Lewy number of 0.18. The code has been successfully applied to resolve FA (Peng *et al.* 2018; Zhao *et al.* 2023*a*,*b*), detonation propagation, supersonic combustion (Cai *et al.* 2017, 2018; Peng *et al.* 2019; Wang *et al.* 2020) and RDE (Yuan *et al.* 2019; Luan *et al.* 2022) simulations.

Concerning the chemical reaction, the FA, DDT and detonation combustion include a wide range of pressures (0.9–100 bar) and temperatures (280–3500 K), hence such a wide range makes it difficult to predict the simulation. However, the hydrogen–air mechanism

proposed by Burke *et al.* (2012) gives a good prediction of the ignition delay time in such a wide range of temperatures and pressures. The hydrogen–air chemical reaction of Burke *et al.*'s (2012) mechanism includes 11 species and 27 steps. The detailed species contain H_2, O_2, H_2O, H, O, OH, HO_2, H_2O_2, N_2, CO and CO_2. All reaction rates are built on the Arrhenius-type equations of (2.6). The specific details can be found in the original references. Such a hydrogen–air reaction mechanism is also similar to the San Diego mechanism (Boivin *et al.* 2011). The ignition delay time has been widely verified in previous literature when coping with the wide range of temperature and pressure combustions for the FA and detonation simulations (Ogawa, Gamezo & Oran 2013; Han *et al.* 2020). The current Burke *et al.* (2012) hydrogen–air mechanism has been extensively employed for FA, DDT and detonation simulation in previous literature (Haghdoost *et al.* 2020; Li *et al.* 2021; Fan & Xiao 2022; Zhao *et al.* 2023*a*,*b*). In addition, Burke *et al.*'s (2012) chemical reaction mechanism has been implemented into the AMROC framework, and we have also successfully employed it in our former FA and DDT simulation (Zhao *et al.* 2021, 2022*a*, 2023*b*, 2024).

To validate the numerical model for handling FA and DDT related to shock waves, AMR and chemical reactions, we conducted validation simulations and compared them with experimental results. These simulations included shock-induced combustion under supersonic flow and FA and DDT within a solid-laden chamber. Additionally, we performed tests on three-dimensional (3-D) simulations of FA and DDT with transverse jets. Detailed results of the verified cases can be found in Appendices A–C.

2.4. *Mesh resolution test in flame acceleration and DDT*

An initial grid size of 4900×100 is utilized to discretize the computational domain, introducing the same mesh resolution in the x and y directions as $\mathrm{d}x = \mathrm{d}y = 2.0 \times 10^{-4}$ m. The governing equations were resolved in the AMROC deploying AMR. Furthermore, mesh resolution tests for FA and DDT simulation in the premixed mixture were conducted here, focusing on T_{DDT} and L_{DDT}. Three different refinement levels and refinement factors of L3 (2, 2), L4-1 (2, 2, 2) and L4-2 (2, 4, 2) were considered, generating a maximum refined mesh sizes of 5.0×10^{-5} m, 2.5×10^{-5} m, 1.25×10^{-5} m, respectively, corresponding to meshes A, B and C. Note that a slightly high ignition pressure for hot spots is utilized to ignite the mixture. The axial positions of the flame front during the FA and DDT in three different mesh resolution cases are superimposed in figure 2, where the DDT occurs at points A, B and C, respectively. It is observed that the flame front position in mesh B and mesh C almost collapsed into one with time evolution. There is a 2.36 % deviation of T_{DDT} in the case of mesh B compared with mesh C, as shown at points B and C, but L_{DDT} values in mesh B and mesh C are almost the same. Additionally, the obtained result also demonstrates that the DDT mechanism is the same in the L4-1 and L4-3 cases. Consequently, the mesh resolution in the fourth level, L4-1, is sufficient to resolve the FA and DDT.

These mesh resolution test results are consistent with former research on DDT simulations (Gamezo *et al.* 2007, 2008; Kessler, Gamezo & Oran 2010). More recently, Xiao & Oran (2020) also reported that more than 10 cells per laminar flame thickness and 5 cells per half-reaction thickness were enough to deal with all flow and flame propagation characteristics associated with FA and DDT, and the corresponding DDT mechanism could also be obtained adequately. Our previous DDT studies also confirmed this (Zhao *et al.* 2023*b*, 2024).

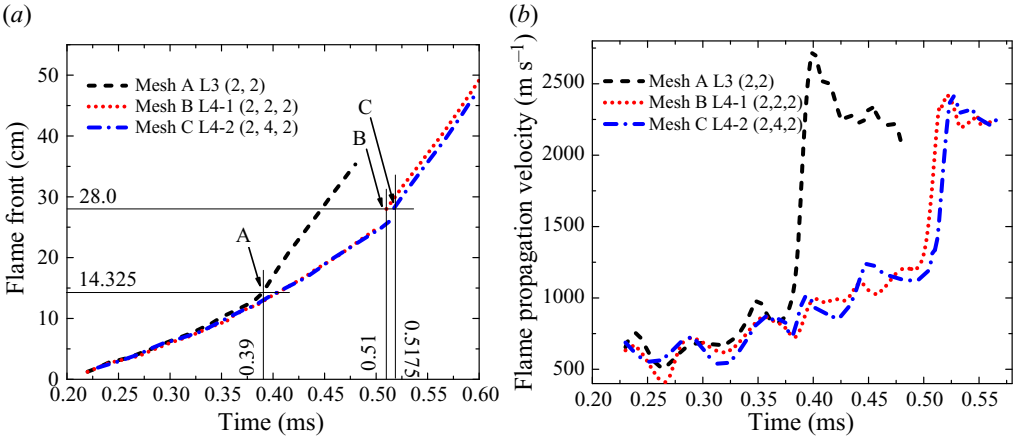

Figure 2. The (*a*) flame front position and the corresponding (*b*) flame front propagation velocity with time evolution for three mesh resolution cases.

The mesh resolution in L4-1 generates 14.4 cells per laminar flame thickness. As such, to balance the computing resource and simulation accuracy, the fourth level, L4-1, is employed for the current simulations having large time and space scales (1 m), generating 31.36 million cells using a uniform mesh under the current mesh resolution.

It is worthwhile mentioning that the computational mesh is dynamically refined by the AMR technique, which is mainly controlled by two threshold criteria. The first criterion of the surrounding cell differences of a scalar quantity is applied to the temperature, pressure and density, while the second criterion of estimating the local truncation error by Richardson extrapolation is employed for the species mass fractions. Detailed AMR threshold selections are given in Appendix B. All cases listed in table 2 were computed using the Tianhe-1 supercomputer, utilizing 660 cores for the computations. Each case required approximately 220 000 cpu × h.

3. Results and discussion

3.1. *Flame acceleration and DDT in the supersonic mixture*

3.1.1. *Mixing process*

The mixture generally has a non-uniform state with temperature, pressure and ER gradients (Boulal *et al.* 2016) in practical detonation-based engines. Here, considering a more realistic engine, the mixing process is simulated under the supersonic air flow and transverse fuel injection before the mixture ignition. The mixing process time is set as $t = 0.84$ ms, and two groups of transverse fuel jets with high stagnate pressure are injected into the chamber, as presented in figure 1(*b*). As a result, an inhomogeneous hydrogen–air mixture is generated in the combustion chamber under the influence of the main supersonic flow. The snapshots of the mass fraction of H_2 during the mixing process under the main flow are given in figure 3. Thanks to the high dynamic pressure of the main flow, the fuel jet is deflected rapidly because of the low dynamic pressure ratio between the fuel and air. As a blockage effect is generated by the fuel jets, the penetration depth is gradually increasing. With the aid of Kelvin–Helmholtz (K-H) instability, vast fuel vortices propagate in the downstream chamber. Under the influence of the flow instability and diffusion effect, the uniformity of the hydrogen–air mixture is augmented. Since a high *Br* and low diffusion

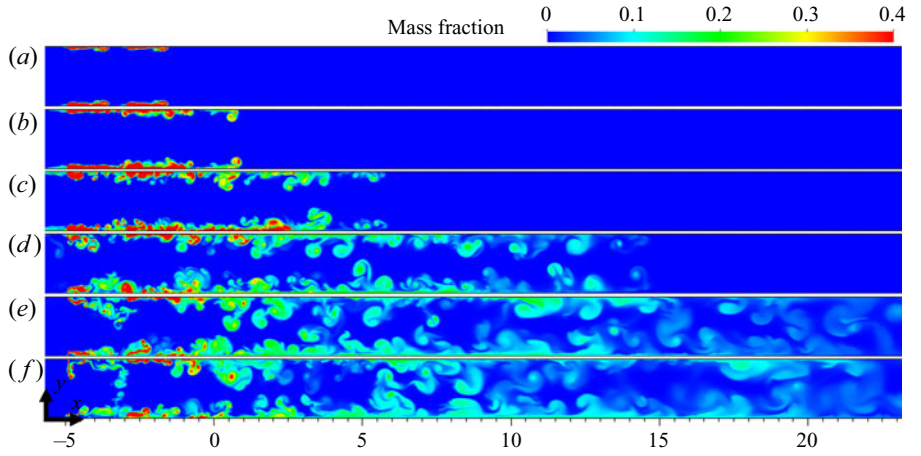

Figure 3. Variations of H_2 mass fraction during the mixing process under supersonic incoming air: (*a*) $t = 0.22$, (*b*) $t = 0.26$, (*c*) $t = 0.34$, (*d*) $t = 0.50$, (*e*) $t = 0.70$ and (*f*) $t = 0.82$ ms.

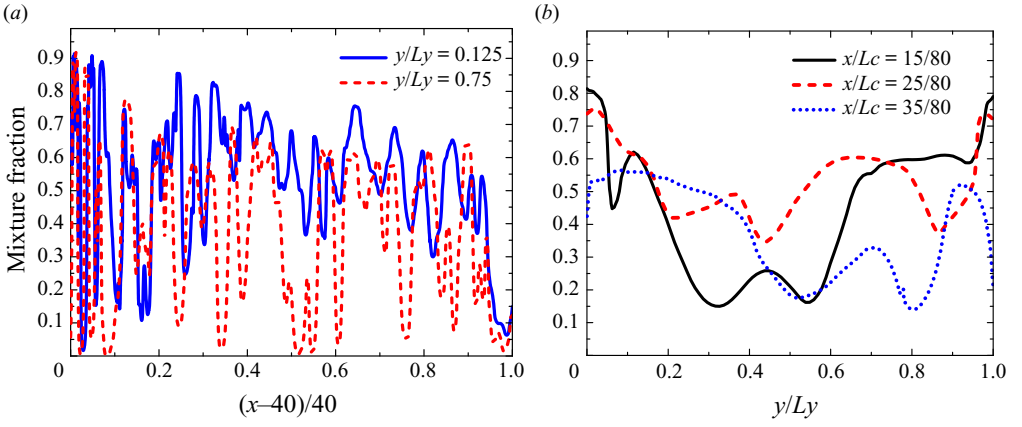

Figure 4. The mixture fraction distribution in the (*a*) horizontal and (*b*) transverse dictions at the end of the mixing process.

effect is formed in the 2-D simulation, a high mass fraction of H_2 in the upper and lower walls is observed.

After the end of the mixing process, the distributions of mixture fraction along the horizontal and transverse directions in the selected domain of $x = 0$–40 cm are plotted in figure 4. The mixture fraction is defined as follows:

$$f = \frac{(1/2M_H)(Y_H - Y_{H,2}) - (1/M_O)(Y_O - Y_{O,2})}{(1/2M_H(Y_{H,1} - Y_{H,2})) - (1/M_O)(Y_{O,1} - Y_{O,2})}, \tag{3.1}$$

where M denotes molecular weight, Y represents elements mass fraction and subscripts 1 and 2 denote fuel jet and incoming air, respectively. Note that the molecular and mass fraction of H in the fuel jet is 1, while the molecular and mass weight of O is 0.

In figure 4(*a*), a highly fluctuating value is formed in the chamber between 0 and 1, while with the mixing propagating into the downstream chamber, the uniformity of the mixture is augmented. In the transverse direction, the mixture fraction still has a lot of

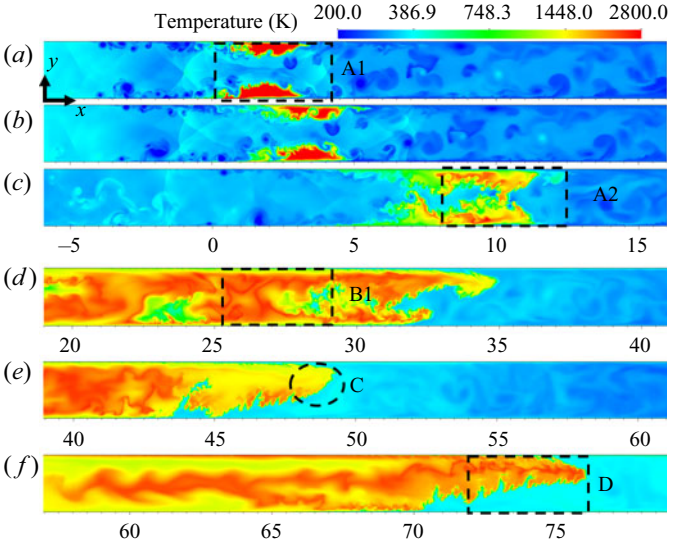

Figure 5. Snapshots of the temperature contours during the FA in the inhomogeneous supersonic mixture without transverse jet obstacles (case 3): (*a*) $t = 1.09$, (*b*) $t = 1.12$, (*c*) $t = 1.24$, (*d*) $t = 1.54$, (*e*) $t = 1.70$ and (*f*) $t = 1.95875$ ms.

fluctuations even in the downstream tube, and the mixture fraction value is in the range of 0.2–0.6. There is a more uniform mixture in the central domain of the chamber in contrast to the upper and lower walls. Part of the reason is that this is a 2-D simulation without a 3-D influence that has a larger diffusion effect and lower *Br*. Generally, the mixtures in the horizontal and transverse directions have high-concentration gradients and are far from the stoichiometric state.

3.1.2. *Global flame acceleration characteristics*

After the completion of the mixing process, the combustion evolution in the inhomogeneous mixture without fluid obstacles is depicted in figure 5, corresponding to case 3. At $t = 1.09$ ms, two regions with high temperatures are formed in the upper and lower walls, attributed to the hot spot ignition. The lower-temperature areas in figure 5(*a*) indicate the presence of fuel vortices. As seen in box A2, a substantial number of lower-temperature products are generated with the highly turbulent flow since there are a lot of fuel-rich mixtures due to the K-H and Rayleigh–Taylor (R-T) instabilities. Nevertheless, the combustion temperature significantly decreases (box A2), caused by the high H_2 concentration in the upstream chamber. As the flame propagates, the temperature increases from 1700 to 2400 K; see box B1, owing to the turbulent mixing reaction, while the temperature in the flame tip is still low (circle C in figure 5*e*). The temperature distribution in the combustion product is, therefore, extremely uneven. Next, with the flame front further propagating, it elongates steadily, and the combustion temperature is increased; see box D in figure 5(*f*), and therefore, the unburned mixture is preheated due to the increasing intensity of the LSW. However, the detonation transition fails because of the long-time FA and dramatically inhomogeneous mixture.

Referring to the former literature (Peng *et al.* 2018; Zhao *et al.* 2023*a*), to activate DDT, the jet obstacles are employed in the premixed mixture to stimulate DDT. Four groups of transverse jets are utilized (case 2). The temperature variations are given in

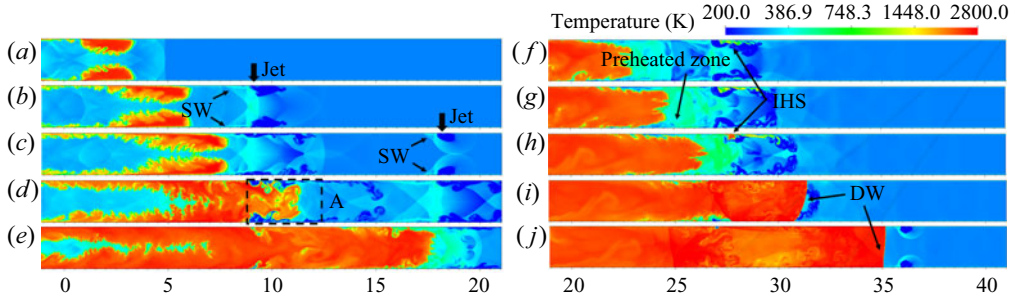

Figure 6. Time sequence of temperature fields showing the propagation of the flame–turbulence, flame–shock and shock–shock interactions during the FA and DDT in case 2. SW-shock wave, IHS-auto-ignited hot spot, DW-detonation wave: (*a*) $t = 0.2450$, (*b*) $t = 0.2750$, (*c*) $t = 0.3200$, (*d*) $t = 0.3800$, (*e*) $t = 0.4550$, (*f*) $t = 0.5000$, (*g*) $t = 0.5150$, (*h*) $t = 0.5300$, (*i*) $t = 0.5450$ and (*j*) $t = 0.5600$ ms.

figure 6. After the jet is injected into the chamber, a perturbed penetration and oblique shock wave are formed, preheating the unburned mixture. Furthermore, when the flame front propagates in this region, the transverse jet also provides a blockage effect to some degree as a solid obstruction. The flame–turbulence interaction is observed accordingly, resulting in a conspicuously increasing flame surface area (box A). Influenced by K-H and R-T instabilities, a corrugated flame front is generated, feeding back to the FA (Gamezo *et al.* 2008).

Consequently, the LSW is strengthened, causing a preheated zone with high temperature at $t = 0.5000$ ms. The third group of the transverse jets is deflected by the main flow, and an auto-ignited hot spot is generated as manifested in figure 6(*f–h*) as a result of the intensive shock wave. Consequently, the onset of detonation occurs because the hot spot ignition evolves into detonation combustion at the upper boundary wall. This DDT mechanism is caused by the flame-kernel ignition through shock–boundary interaction, as reported in Goodwin's study, where a slightly higher *Br* was employed (Goodwin *et al.* 2016). Such a DDT mechanism is also reported in Grogan & Ihme's (2015, 2017) studies and it is found that the detonation transition though the flame-kernel ignition is due to the shock wave amplification by coherent energy release (SWACER) mechanism. Finally, the detonation wave propagates into the downstream chamber, as shown in figure 6(*i*,*j*).

The transient temperature contour and the corresponding AMR distribution in case 2 are given in figure 7. The AMR works well in large temperature and pressure gradients, especially in the regions having shock wave, flame front and jet obstacles. These AMR regions also dynamically move as the flame tip and shock wave evolve. Hence, the current AMR threshold values are sound.

Additionally, a comparison of the flame tip versus time in case 1 and case 2 is plotted in figure 8. The flame front position in the premixed mixture without a jet is larger than the case with the transverse jet in the incipient stage. This is due to the *Br* influence stemming from the transverse jet when a host of fluids is injected into the chamber, introducing a high-pressure region at the beginning of the flame front, which has a negative influence on FA at the initial time. This result is also reported in our previous study (Zhao *et al.* 2022*a*).

By contrast, the transverse jets provide vast perturbed vortices and a moderate *Br*, introducing plenty of flame–turbulence, flame–shock and shock–shock interactions and increasing the flow instabilities and the flame surface area, as discussed above. Subsequently, the deflagration flame evolves into detonation rapidly, as marked by circle A. Therefore, in the later stage, many transverse jets ejecting into the supersonic mixture benefit DDT when the flame front approaches the perturbed region. This is consistent with

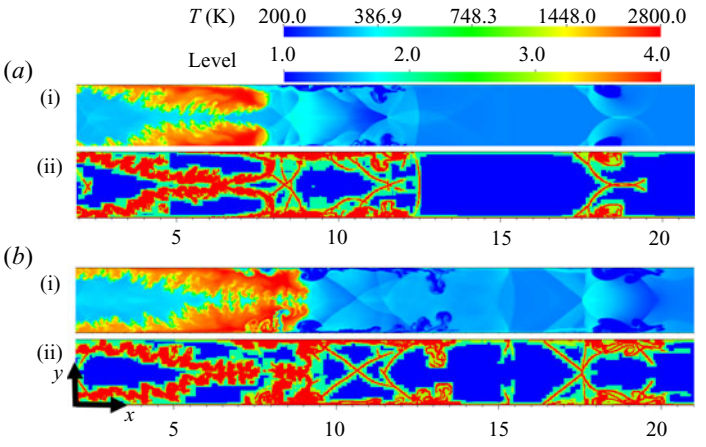

Figure 7. The transient temperature contour and the corresponding AMR distribution: (*a*-i) $t = 0.37$ and (*b*-i) $t = 0.40$ ms.

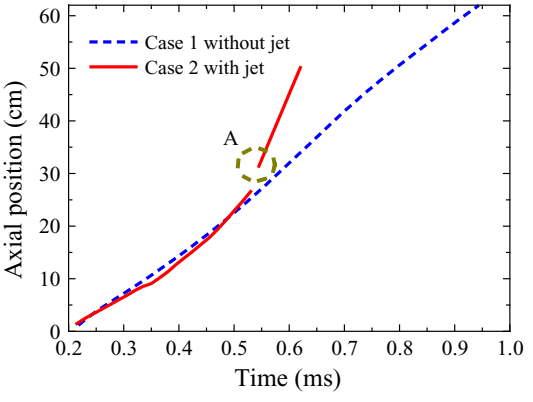

Figure 8. Evolution of axial position of the flame front in the cases for premixed mixtures with and without transverse jet obstacles.

the previous research where one transverse jet obstacle is adopted in the static mixture (Frolov *et al.* 2017; McGarry & Ahmed 2017; Peng *et al.* 2018; Cheng *et al.* 2021*a*). Furthermore, the present jet obstacles further introduce an oblique shock wave due to the supersonic flow, which is more reliable in increasing the intensity of the FA and LSW (Zhao *et al.* 2023*a*).

Consequently, inspired by case 2, four groups of head-on jets are also employed in the inhomogeneous supersonic mixture. To increase the uniformity of the mixture, the jet obstacles are composed of air. The FA and detonation transition snapshots are given in figure 9. The temperature variations in incipient time are similar in the above case. The combustion temperature is significantly as low as 1800 K; see box A1.

Nevertheless, as the air jets are injected into the chamber, as seen in figure 9(*c*), oblique shock waves form. An apparent flame–turbulence interaction is observed when the flame reaches the air jet regions (see figure 9*d–f*), increasing the flame surface area dramatically, and then the flame speed augments accordingly. Furthermore, the combustion temperature is increased to 2700 K (boxes B1 and B2) due to the increasing uniformity of the mixture when introducing a lot of perturbed jet flows. As a result, preheated zones are generated

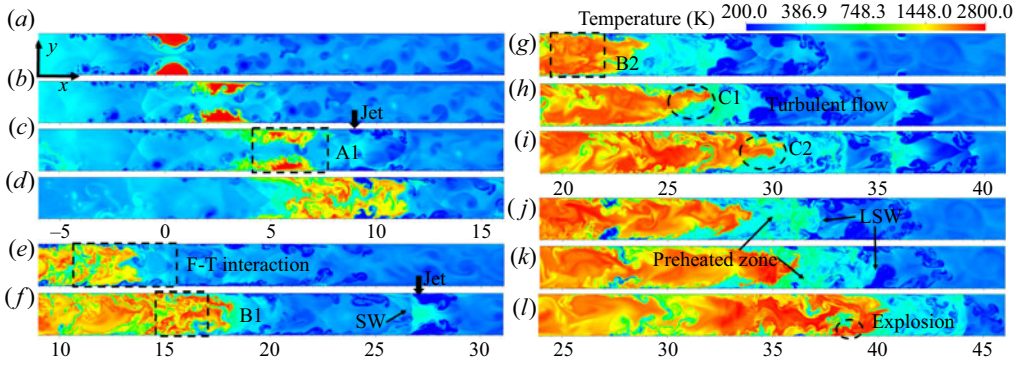

Figure 9. Snapshots of the temperature fields during the FA and DDT under the influence of transverse jet obstacles (case 4). F-T – flame-turbulence, SW – shock wave, LSW – leading shock wave: (*a*) $t = 1.06$, (*b*) $t = 1.105$, (*c*) $t = 1.165$, (*d*) $t = 1.255$, (*e*) $t = 1.285$, (*f*) $t = 1.345$, (*g*) $t = 1.405$, (*h*) $t = 1.435$, (*i*) $t = 1.475$, (*j*) $t = 1.5225$, (*k*) $t = 1.53125$ and (*l*) $t = 1.570$ ms.

ahead of the flame tip because of the strong shock wave. Many shock waves focus on and collide with the oblique shock wave generated by the transverse jet. These features result in prominent preheated zones, as shown in figure 9(*g–i*). The elongated flame front (circle C) generates a dramatically increased flame surface area, resulting in a high energy release ratio (Gamezo *et al.* 2008) and a significantly increased combustion temperature in contrast to figure 5 without jet obstacles. A stronger LSW is formed subsequently. The LSW preheats the turbulent jet, as figure 9(*i–k*) shows. Finally, a localized explosion point is formed against the lower wall, as figure 9(*i*) shows. Detailed information on the DDT and the subsequent detonation propagation will be discussed in §§ 3.3 and 3.4.

For the sake of revealing the failure of the DDT in the premixed and inhomogeneous mixtures without transverse jet obstacles, the positions of the flame front, LSW and the corresponding flame front propagation velocity are superimposed in figure 10(*a*,*b*), respectively. The FA in the premixed supersonic mixture can be classified into four stages. Stage I (0.2–0.33 ms): the flame front propagation velocity is decreased rapidly due to the influence of the supersonic flow. When it is close to the flow speed of the unburned mixture, the flame front goes into stage II (0.33–0.58 ms), and the flame propagation speed continues to increase as the flame surface area increases. In the next stage (0.58–0.68 ms), the flame propagation speed remains stable, which can be considered as a deflagration flame because its speed approaches half of the CJ speed. It is observed that the speed is around 1000 m s^{-1}, which is also close to the speed of sound in the combustion products. This means that DDT usually occurs when the flame tip propagation speed is close to the speed of sound in the product gas because there is no continuous transition from the deflagration combustion in the lower branch to the detonation model along the Hugoniot curve (Zhao *et al.* 2022*a*, 2023*b*).

Nevertheless, after that, due to the lack of flow instability and blockage effect within the smooth chamber and an increasing length between the flame tip and LSW (L_{fs}), the flame propagation speed decreases steadily. Hence, as reported in former DDT simulations (Oran *et al.* 2020; Gamezo *et al.* 2021), a constant L_{fs}, namely, the situation of a shock–flame complex (Gamezo *et al.* 2008; Oran *et al.* 2020), is an essential condition to activate the detonation transition. In contrast, an increasing L_{fs} results in a failure of detonation initiation. As such, DDT is difficult to form in a deflagration flame within a smooth

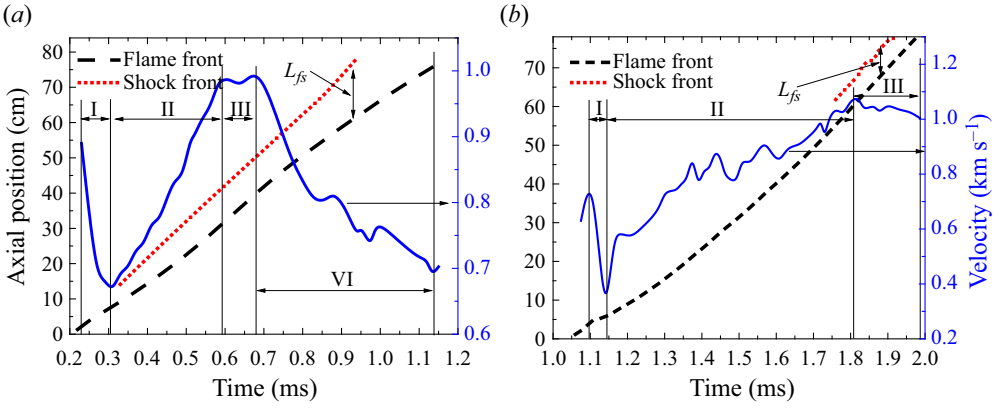

Figure 10. The positions of the flame front, LSW and the corresponding flame propagation velocity as a time sequence in the (*a*) premixed (case 1) and (*b*) non-uniform (case 3) supersonic mixture. The blue curve denotes the flame front propagation velocity.

tube despite being in a premixed supersonic mixture without considering a perturbation configuration.

In figure 10(*b*), flame propagation in the inhomogeneous mixture can be classified into three stages without stage VI in the inhomogeneous mixture. Stage I is the ignition time, and it has a high flame propagation speed but reduces abruptly owing to the extremely fuel-rich mixture. Under the effect of the main flow, the flame–turbulence interaction increases again in stage II. In stage II, the propagation speed continues to increase as time evolves, whereas the required time is increased from 0.3 ms to 0.6 ms compared with the FA ratio in the premixed mixture as plotted in figure 10(*a*); hence, the increasing ratio of the flame propagation speed is reduced and has more fluctuation. After that, in stage III, the flame speed approaches half of the CJ value, whereas its speed slightly decreases as L_{fs} increases. Hence, the detonation transition is still a failure.

3.2. *Comparisons of flame structure in the premixed and inhomogeneous mixtures*

In this part, the FA and the flame front structure between the premixed and inhomogeneous mixtures that occurred in case 1 and case 3 are discussed here. The details of the flame propagation in both cases are also investigated to elucidate the factors contributing to the failure of the DDT.

3.2.1. *Premixed mixture*

In the incipient stage of the FA in the premixed supersonic mixture for case 1, a typical flame front structure and the corresponding temperature variation at $t = 0.3100$ ms are given in figure 11. A breached flame tip is formed due to the two hot spot ignitions in the upper and lower walls, which subsequently merge in the middle region. Analysis of species mass reveals that the HO_2 radical forms early in the front of the flame structure, followed by O, H and OH, initiating a chain-branching chemical reaction. In contrast, the peak value of HO_2 is a lower order than the peak value of H, O and OH radicals. The peak mass fraction of HO_2 reaches 1.5×10^{-5}. As it is depleted rapidly, the concentrations of H, O and OH are increased significantly, accomplished by an increasing temperature from 306 to 2000 K; hence, the chain-branching chemical is continued through the consumption

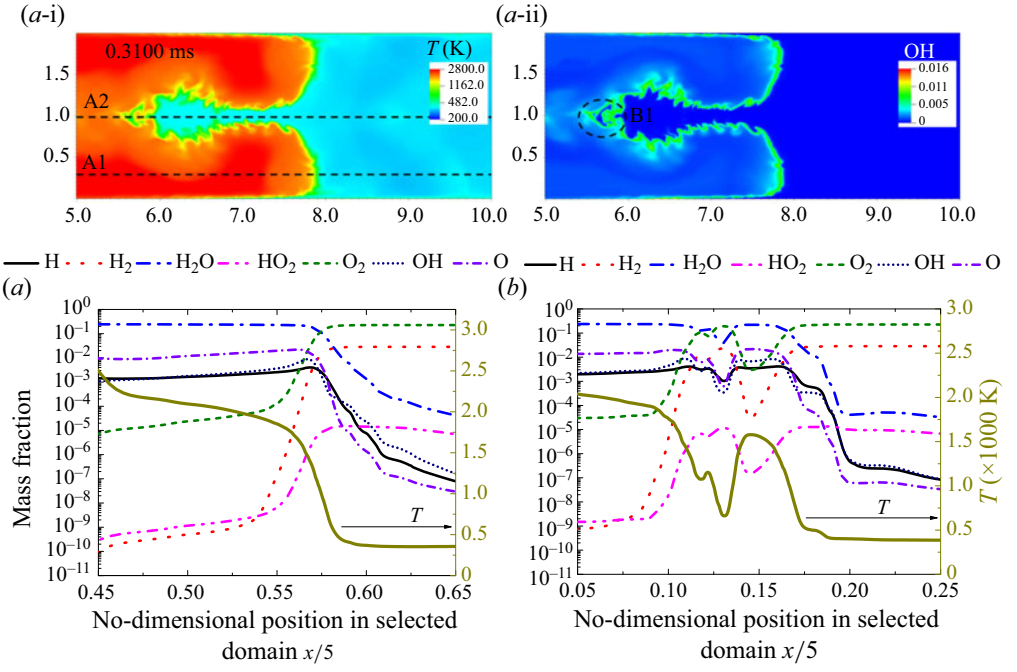

Figure 11. Variations of temperature and species mass fraction across the flame front (*a*) near the wall and (*b*) middle region at the incipient FA for the premixed mixture in case 1 ($t = 0.3100$ ms).

of HO_2 and H_2O_2. The peak value of H, O and OH radicals reach 0.0039, 0.0217 and 0.0087 with the mass fraction of H_2 and O_2 decreasing through the branching reactions of $H + O_2 = O + OH$ and $O + H_2 = H + OH$. As a result, the active reaction zone is around a range between 0.525 and 0.60, which has a single layer. This flame front structure is in agreement with that of a premixed flame, as discussed by Law (2010). In the middle region of the flame front structure, due to the flow instability, some residual mixture exists in the downstream product; see circle B1 in figure 11(*a*2). Thus, the flame front structure is more complicated, and the reaction front has two layers. As a result, there is a hump in the variations of species mass fraction and temperature curves.

As the flame front further propagates into a stable state with maximum flame propagation speed, typical flame structures in the premixed mixture, including the species mass information at different flame positions at $t = 0.6800$ ms, are plotted in figure 12. A lot of wrinkled flames appear in the flame front. Figure 12(*a*,*b*) gives the mass fractions at $y/Ly = 0.125$ and 0.625, corresponding to lines B1 and B2, respectively. The species curves show the same result: the HO_2 forms early in the front of the flame structure, followed by H and O, resulting in main chain-branching reactions and mixture burning.

Furthermore, as the mass fraction of HO_2 reaches a peak value of 3.2×10^{-4}, it is consumed sharply, with the mass augmentations of OH, O and H to peak values of $O = 0.018$, $H = 0.0037$ and $OH = 0.009$. Hence, the chain-branching reactions keep going, forming a gradual increase in H_2O product and an abrupt decrease in H_2 and O_2. Thus, the energy release ratio increases, increasing the combustion temperature from 428 to 2200 K. Due to the much higher pressure and temperature in the preheated mixture, the flame thickness of 1.2×10^{-3} m is much lower compared with the initial stage.

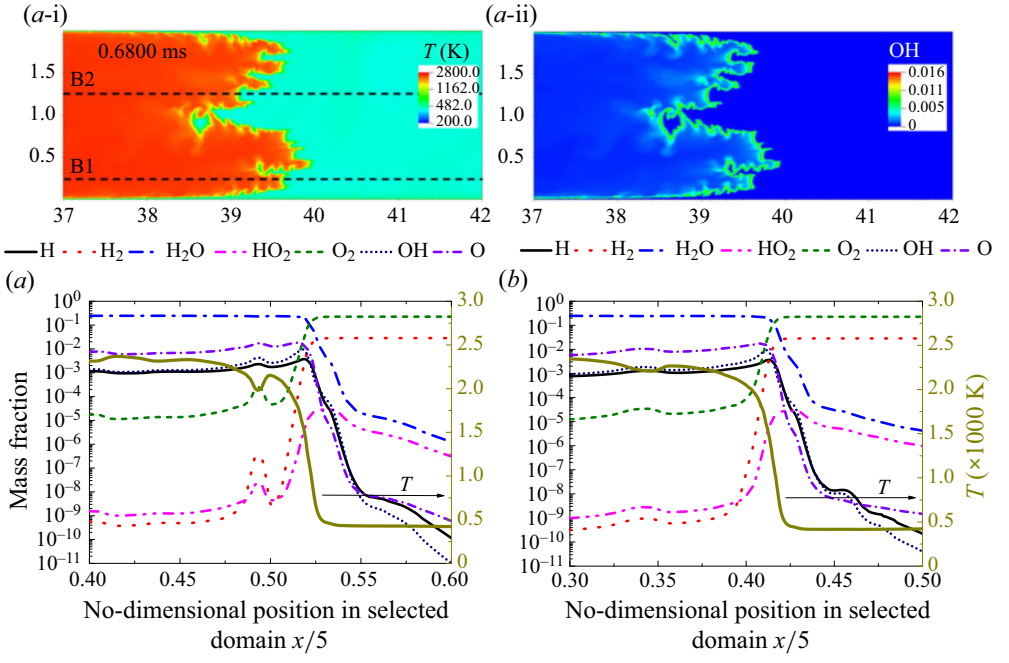

Figure 12. Variations of temperature and species mass fraction across the flame front in (*a*) lower (0.25/2.0) and (*b*) upper (1.25/2.0) regions at the incipient FA in case 1 at $t = 0.6800$ ms.

In contrast, the grid resolution can still achieve 48 points per flame thickness, which is sufficient to resolve the combustion characteristics. At the flame position $y/Ly = 0.625$, the species mass fraction is similar to that at $y/Ly = 0.125$. The HO_2 mass fraction appears early at the flame tip, followed by the H, O and OH radicals. With the rapid consumption of HO_2, H_2 and O_2, the OH and product of H_2O increase, leading to an increase in the combustion temperature.

3.2.2. *Inhomogeneous supersonic mixture*

Concerning the FA in the inhomogeneous supersonic mixture in case 3, the flame structure information at $t = 0.1540$ ms, around the two finger flame tips ($y/Ly = 0.125$, 0.75), is shown in figure 13. In the lower flame structure, the mass fraction is hugely uneven. In the flame tip, the HO_2 radical appears first, followed by H, O and OH, with the mass fraction of HO_2 augments, resulting in the increased temperature from 327 to 1420 K. But the increased ratio of the temperature is relatively lower than that in the premixed mixture. Much unburned H_2 is still left behind with a high mass fraction of $H_2 = 0.01$. As such, the second combustion layer continues in the downstream product so that another flame structure layer with a hump shape appears downstream. With the HO_2 increasing again, accompanied by the increases of H, O and OH radicals, the mass fractions of H_2 and O_2 are subsequently consumed rapidly, further increasing the temperature to 2010 K. The combustion process is, therefore, more complicated in contrast to the premixed mixture. Hence, the temperature contour near the lower wall exhibits an extreme maldistribution.

Line A2 has just one layer of the flame front structure. The species mass fraction shows that the peak values of H and O are 0.0072 and 0.0018, respectively, so that the H mass fraction is almost two times that of the premixed mixture due to the fuel-rich

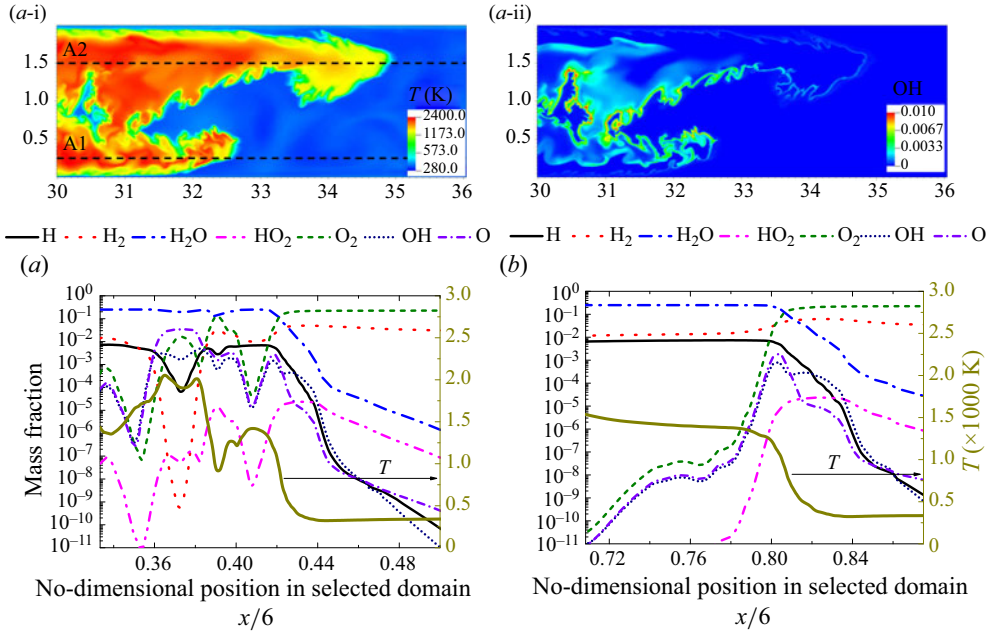

Figure 13. Variations of temperature and species mass fraction across the flame front in (*a*) lower (0.25/2.0) and (*b*) upper (1.5/2.0) regions during FA for the inhomogeneous mixture in case 3 ($t = 0.1540$ ms).

mixture. Thereby, a significantly lower peak value of OH mass fraction of 0.00078 appears, contributed by the lack of O_2. Hence, this results in an extreme fuel-rich reaction, leading to a lower increased temperature from 325 to 1380 K. Consequently, many unburned fuels are left behind in the downstream chamber with a high mass fraction, $H_2 = 0.014$. Due to the fuel-rich combustion, a large flame thickness is generated when compared with the premixed mixture.

Figure 14 further gives more detailed information on the temperature, hydrogen, ER and flame front structure with species information along the y-direction position at $t = 1.54$ ms. To picture the variation of temperature, hydrogen, ER and the radical element distribution, 3-D plots are presented on the right side, where the x-axis is in a range of from 30.0 cm to 36.0 cm, while discrete y-axis coordinates are selected at 0.25, 0.5, 0.75, 1.25. 1.5 and 1.75 cm. The corresponding specific values are plotted in the z-axis direction of the 3-D plot.

A high fluctuation of the temperature distribution is observed after the flame front, especially in the regions near the lower and upper walls. A gradually increased temperature is noted near the upper and lower walls. Hence, the combustion reaction is still continued in the downstream product. Although there is a much larger flame front surface area than in the premixed mixture, the temperature at the front is still significantly lower. In Zheng *et al.*'s (2019) study, the FA occurred in an ER gradient normal to the flame propagation direction, and they also found that there is a larger surface area in the inhomogeneous mixture compared with the homogenous mixture, but this does not result in a high energy release ratio. This is due to the large surface area mainly located in the fuel-lean regions. Therefore, the temperature highly depends on the ER distribution.

As shown in the H_2 and ER maps, the upper wall has a much thicker fuel layer, and the ER distribution is highly uneven. A high fuel-rich condition exists in the upper half-domain, and the ER value is around 2.5. Yet, a much lower fuel concentration is

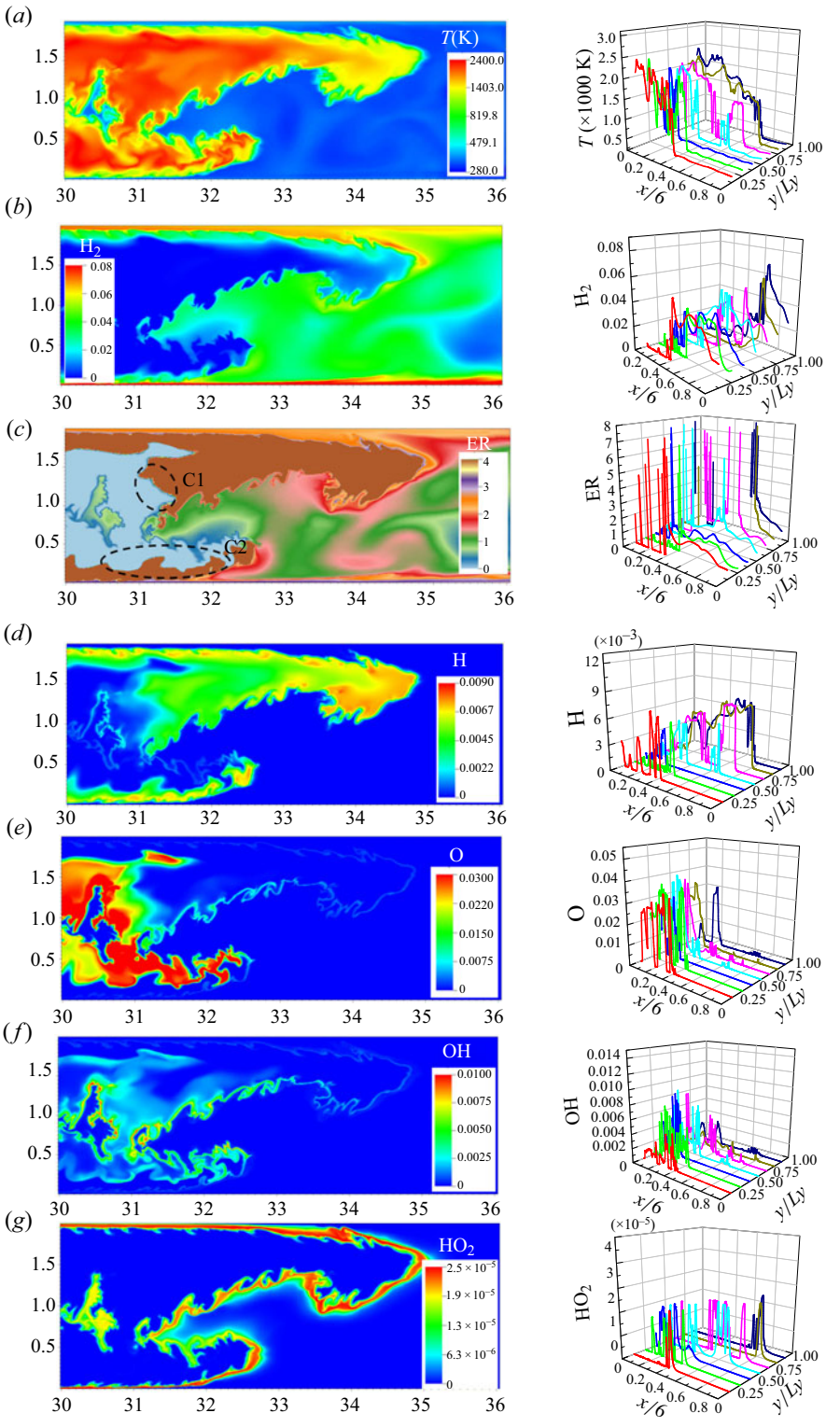

Figure 14. The (*a*) temperature, (*b*) equivalation ratio (*ER*) and flame (*c–g*) front structure distribution at $t = 0.15400$ ms for the inhomogeneous supersonic mixture (case 3) along different horizontal positions in the *y*-direction.

observed near the middle domain (ER is approximately 0.8), resulting in two colour distributions in the combustion product. The ER map of the combustion product includes grey (ER = 0) and brown (ER = ∞), representing that the fuel and oxidizer have been consumed, respectively. The H, O and OH mass fraction distributions also yield a high fluctuation in the downstream combustion. There is a high mass fraction of H in the upper combustion product, while a high O mass fraction is formed in the lower combustion product. Such a feature further leads to a local reaction in the downstream tube due to a further mixing process between the H_2 and O_2, especially in the connecting region between grey and brown; see circles C1 and C2 in figure 14(*c*). The HO_2 concentration mainly occurs in the flame front structure, with a maximum of 2.0×10^{-5}. It is an essential species for initiating induction reaction, and a much thicker induction reaction zone is formed in the fuel-rich layer. Consequently, a much lower temperature occurs in the upper flame front. In general, the temperature contour distribution is particularly uneven.

To sum up, the flame front structure in the inhomogeneous supersonic mixture is more complicated, characterized by multiple reaction layers compared with the premixed mixture. Additionally, the flame thickness in the inhomogeneous mixture is much higher than that in the premixed mixture. The presence of extreme fuel-lean and fuel-rich mixtures with a perturbed distribution results in a significantly lower combustion temperature with a highly uneven distribution, generating a lower FA ratio. However, the combustion temperature is further increased due to the continuous reaction in the downstream flame resulting from the turbulent mixing process.

3.3. *Mechanisms of DDT and detonation reinitiation*

The former experimental and numerical studies have extensively investigated the DDT mechanism and detonation propagation in the premixed mixture (Austin 2003; Radulescu *et al.* 2007; Mahmoudi & Mazaheri 2011, 2015; Mahmoudi *et al.* 2014). In comparison, the successful DDT mechanism, detonation extinction, reinitiation and propagation in a more practical inhomogeneous flow mixture have not been adequately studied, especially in the detonation extinction that occurred in the limited ER region. It is vital for a detonation-based engine, as suggested by Boulal *et al.*'s (2016) experimental research, especially for an engine with non-premixed fuel injection or non-perfect mixing. As confirmed by their suggestion, numerical simulation is a significant tool to reveal these. Hence, the DDT mechanism and detonation propagation in the inhomogeneous supersonic mixture in case 4 are discussed here.

3.3.1. *Mechanism of onset of detonation*

Here, more instantaneous snapshots of the temperature and pressure variations surrounding the explosion point are given in figure 15, corresponding to case 4. A localized explosion point takes place, and it propagates into the downstream lower wall, as seen in the series of circles A. Meanwhile, a high-pressure region is generated in the lower wall accompanied by the detonation wave (see circles B), forming a transverse wave shedding from the detonation front.

To thoroughly picture the mechanism of detonation transition, figure 16 shows the transient variations of temperature, pressure and OH before forming the localized explosion point with a time step of 0.00125 ms. A remarkable shock wave is generated at the lower wall and propagates in the downstream mixture (figure 16*a*2), forming an intense Mach stem subsequently (figure 16*b*2), where the maximum pressure reaches 3.0 MPa. In addition, the fierce shock wave also results in a high combustion temperature

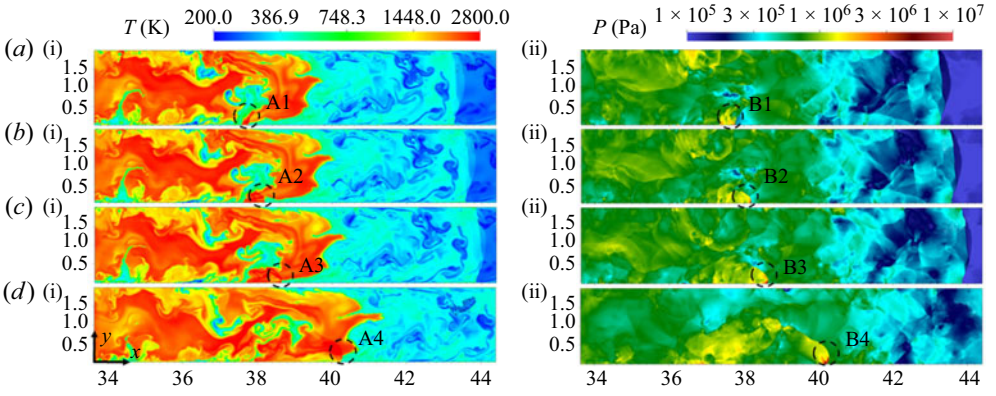

Figure 15. Snapshots of the temperature and pressure contours showing the propagation of the explosion point for case 4: (*a*1) $t = 1.56375$, (*b*1) $t = 1.56625$, (*c*1) $t = 1.56875$ and (*d*1) $t = 1.57500$ ms.

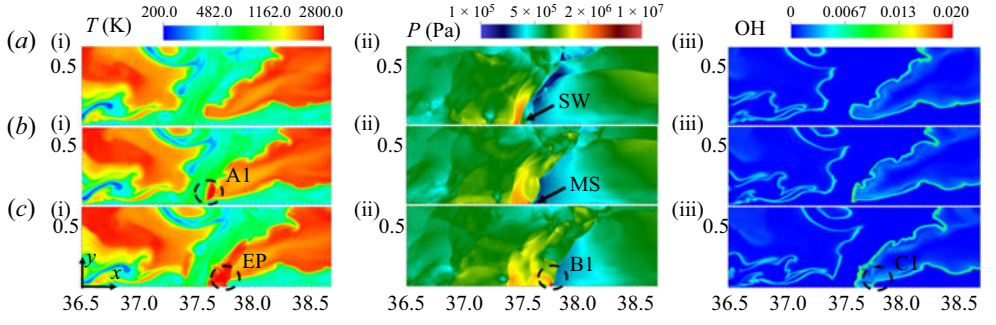

Figure 16. Contours of the temperature, pressure and OH variation illustrating the activation of the onset of DDT in case 4. SW – shock wave, MS – Mach stem, EP – explosion point: (*a*1) $t = 1.56125$, (*b*1) $t = 1.56250$ and (*c*1) $t = 1.56375$ ms.

(circle A1). As a result, a localized explosion point forms in the lower wall (figure 16*c*1), forming a high explosion pressure and OH concentration (circles B1 and C1). The onset of detonation is triggered, propagating in the downstream mixture. Hence, the strong Mach stem is responsible for the current DDT mechanism, which generates a high-pressure and high-temperature spot sufficient for the detonation transition.

Figure 17 presents a schematic depiction elucidating the progression of the shock wave and flame front evolution observed during the DDT initiation, as depicted in figure 16. Preceding the advancement of the flame front, a robust shock wave propagates downstream, with the reflected shock wave rebounding off the lower wall, thereby engendering a Mach stem configuration and thereby inducing a reactive gradient. Following this, a high-temperature explosion point manifests on the upper wall, subsequently evolving into an explosion point. Thus, the inception of the Mach stem structure emerges as a pivotal procedural facet in this phenomenon.

The DDT mechanism is caused by the gradient mechanism (Oran *et al.* 2020). This mechanism is also reported in Gamezo *et al.*'s (2008) and Goodwin *et al.*'s (2016) studies, where a high *Br* was employed in an obstacle-laden chamber, resulting in an intense Mach stem after undergoing a series of FA.

The current DDT mechanism can be further quantitively analysed by the pressure and temperature records, as shown in figure 18, where the red curves represent the temperature,

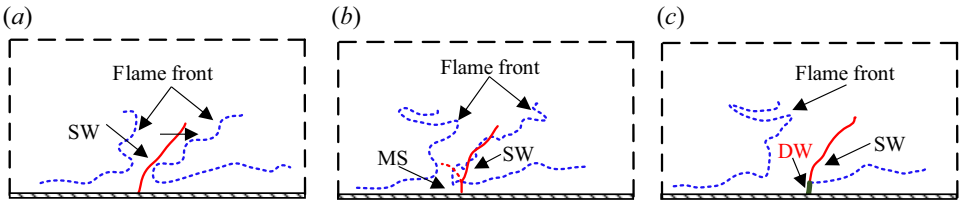

Figure 17. Physical illustration of the shock wave (SW), Mach stem (MS) and flame front evolution during the onset of detonation. DW – detonation wave.

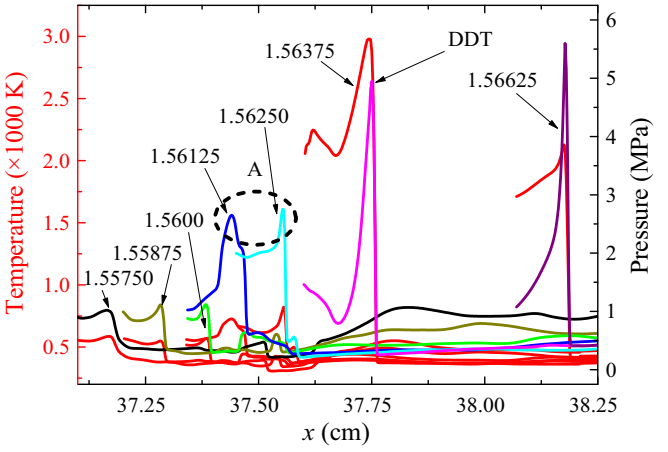

Figure 18. Variations of temperature and the corresponding pressure during the onset of detonation in case 4 along the x-direction in the lower wall, the red lines detonate the temperature. The transient time sequences are $t = 1.5575$ ms, 1.55875 ms, 1.5600 ms, 1.56125 ms, 1.56250 ms, 1.56375 ms and 1.56625 ms.

and the other lines denote the corresponding pressure variations along the x direction along the lower wall. Note that a rapidly increased pressure value from 1.17 to 2.85 MPa (circle A) is formed thanks to the Mach stem; see figure 16(*b*2), and the temperature of the unburned mixture is preheated to 820 K, resulting in a reactive gradient. Under these conditions, the DDT is activated with a localized explosion point with high pressure and temperature values.

3.3.2. *Mechanism of detonation reinitiation*

The next flame propagation is further presented in figure 19. The detonation wave does not survive and is instead extinguished. As illustrated, the detonation wave is decoupled from a flame and a shock wave, as shown in the lower flame front and box A in the temperature and pressure contours, respectively. A gradually reduced temperature and pressure form. As such, a detonation quenching occurs. This is attributed to the extreme fuel-lean mixture in the downstream chamber. As shown in the series of boxes A in the ER map, a significantly lower ER value of around 0.15 exists ahead of the flame front. Such a lower ER distribution is caused by the air transverse jet obstacles located in $x = 36$ cm, which introduce a large amount of air, as presented in figure 9(*j*). As a result, sustained detonation propagation highly depends on a suitable ER.

A donation reinitiation is noted after the flame further propagates into the downstream chamber; see figure 20. First, a remarkable Mach stem is generated against the lower wall; see circle B1. It propagates into the region having a high ER value (circle C2), located

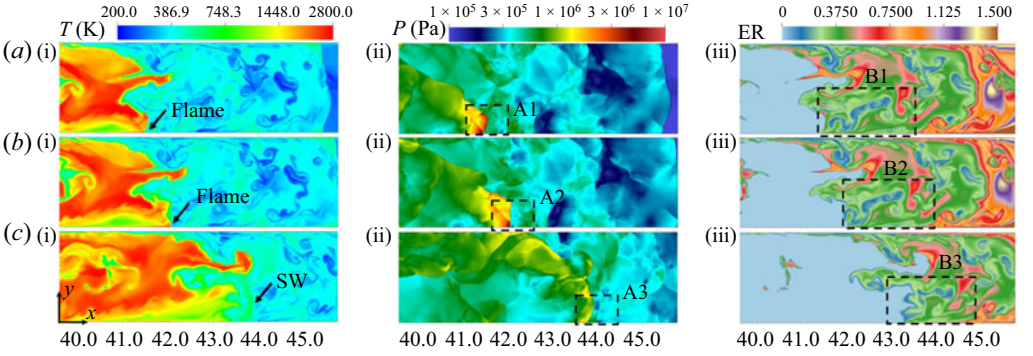

Figure 19. Snapshots of temperature, pressure and corresponding ER in the detonation extinction for case 4. SW – shock wave: (*a*1) $t = 1.58125$, (*b*1) $t = 1.58375$ and (*c*1) $t = 1.59375$ ms.

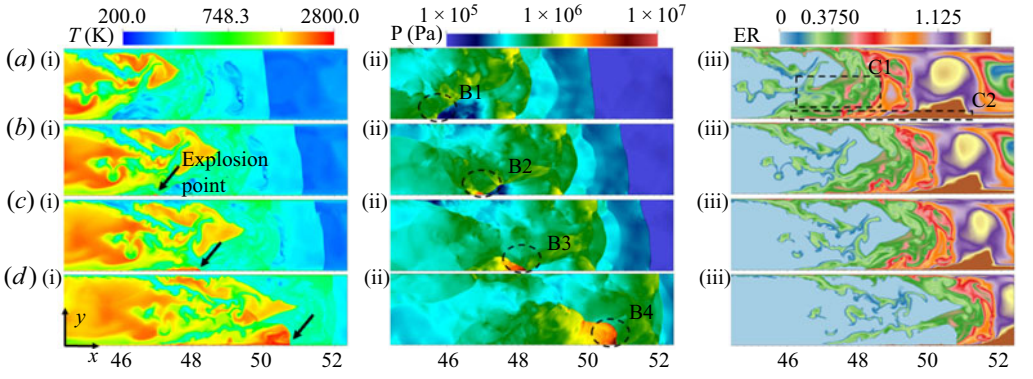

Figure 20. The detonation reinitiation rendered by temperature, pressure and ER evolution in the inhomogeneous supersonic mixture (case 4): (*a*1) $t = 1.61875$, (*b*1) $t = 1.62625$, (*c*1) $t = 1.63125$ and (*d*1) $t = 1.64125$ ms.

in the lower boundary wall compared with the middle part in circle C1. Then, a localized explosion appears (figure 20*b*1), propagating in the lower wall region with a high ER value; see the series of arrows in the temperature contours. Finally, more detonation combustion is formed at $t = 1.64125$ ms where more areas with a high ER mixture exist. Therefore, sustaining detonation highly relies on a continuously suitable mixture. Although there is a quite small and elongated region of the suitable and sensitive mixture, the detonation wave propagation can still survive.

To elucidate the flow structure comprehensively, a schematic representation delineating the evolution of the shock wave, LSW and flame front antecedent to detonation initiation is provided in figure 21. Herein, the blue-coloured region demarcated along the lower periphery signifies a composition conducive to sensitivity. Initially, an incident shock wave propagates downstream adjacent to the bottom wall. Subsequent to this propagation, a Mach stem is engendered, subsequently precipitating the localization of an explosion point. This critical juncture serves as the impetus for detonation combustion, which subsequently propagates throughout the sensitive and elongated region.

The temperature and pressure records during the detonation reinitiation along the x direction from $t = 1.62125$ to $t = 1.63375$ ms are also superimposed in figure 22, where the red curves denote the temperature, and the other lines represent the pressure. Increasing

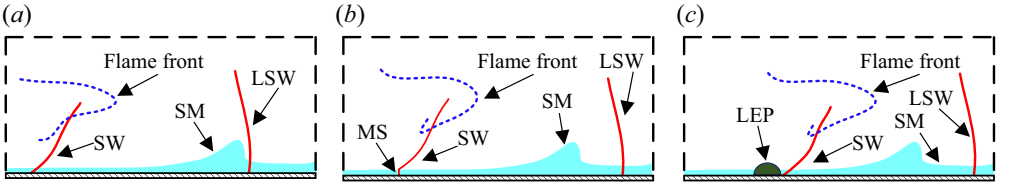

Figure 21. Schematic illustration of the flow structure before the onset of detonation. SW – shock wave, SM – sensitive mixture, LSW – leading shock wave, MS – Mach stem, LEP – localized explosion point.

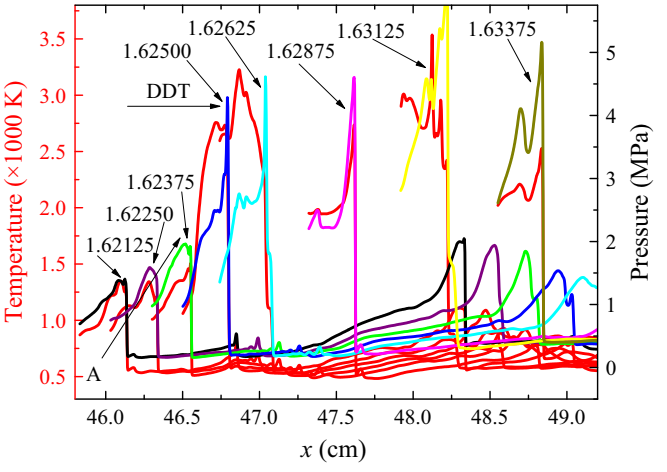

Figure 22. Temperature variations and the corresponding pressure during the detonation reinitiation in case 4 along the x direction in the lower wall. The transient time sequences are $t = 1.62125$ ms, 1.6225 ms, 1.62375 ms, 1.625 ms, 1.62625 ms, 1.62875 ms, 1.63125 ms and 1.63375 ms.

pressure and temperature have occurred; see arrow A, where the peak pressure and temperature reach $T = 1504$ K and $p = 1.95$ MPa at $t = 1.6225$ ms, respectively. Hence, under the high pressure and temperature conditions post-shock, the onset of detonation is triggered at $t = 1.62375$ ms. Next, the detonation propagates downstream (figure 20*d*1). The DDT mechanism is, therefore, the same as the first localized explosion point, as discussed in figures 16 and 17, which is caused by the gradient mechanism because of the intense Mach stem. Such a DDT mechanism is consistent with the result reported by Lee, Knystautas & Yoshikawa's (1980) experiment study, referred to as the SWACER mechanism.

In summary, the inhomogeneous supersonic mixture exhibits more dynamic characteristics, including the detonation transition, quenching and reinitiation, which primarily stem from the extremely inhomogeneous ER distributions. The results indicate that the detonation cannot be sustained when the ER falls below 0.15. The DDT mechanism is ascribed to the Zel'dovich gradient mechanism (Zel'Dovich *et al.* 1970) thanks to a strong Mach stem forming in the boundary wall. As such, in the smooth tube, the DDT mechanism resembles previous numerical and experimental findings, where a robust Mach stem was generated in a solid-laden chamber with a high Br in the FA (Boeck *et al.* 2014; Goodwin *et al.* 2016) and DDT scenarios (Vollmer *et al.* 2012; Zheng *et al.* 2019) occurred in the hydrogen–air or methane–air mixtures. Moreover, the detonation reinitiation mechanism has the same DDT mechanism. Still, the formation of the DDT requires a highly sensitive mixture region so that a discretized low ER

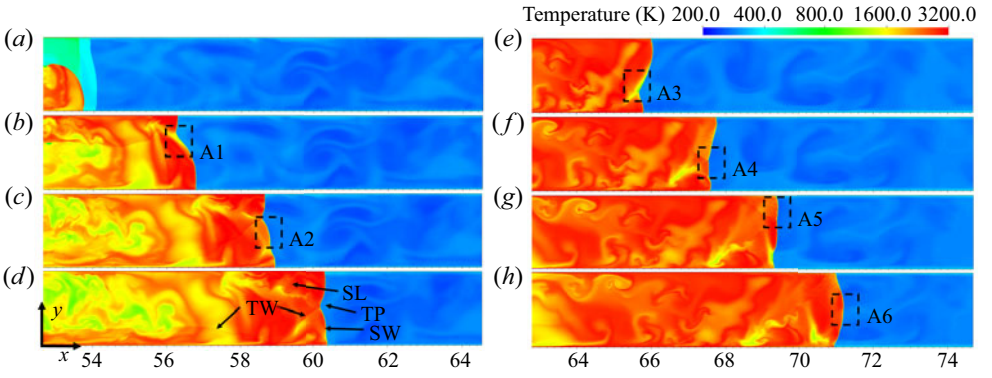

Figure 23. Snapshots of the detonation propagation with temperature evolution in the inhomogeneous supersonic mixture (case 4). TW – transverse wave, SL – slip line, TP – triple point, SW – shock wave: (*a*) $t = 1.65125$, (*b*) $t = 1.6625$, (*c*) $t = 1.67125$ and (*d*) $t = 1.67750$, (*e*) $t = 1.7$, (*f*) $t = 1.7075$, (*g*) $t = 1.715$ and (*h*) $t = 1.7225$ ms.

mixture can be utilized to block the detonation propagation. Yet, the detonation reinitiation can be activated later when the intense shock wave propagates in a highly sensitive mixture.

3.4. *Detonation propagation in inhomogeneous supersonic mixture*

3.4.1. *Global propagation characteristics*

The initial detonation propagation in the supersonic non-uniform mixture is illustrated in figure 23. A smooth flame front scenario is generated owing to the overdriven detonation and low increased temperature ratio between the detonation wave and post-LSW. A sudden lower-temperature region in the leading flame front is formed; see box A1; however, an increased temperature subsequently forms when the detonation wave impacts the upper wall, generating a strong Mach stem. A curved flame appears in box A2.

Besides that, a remarkable transverse wave occurs in the downstream combustion product. A host of vortices appear in the slip line due to the Richtmyer–Meshkov (R-M) instability (Mahmoudi *et al.* 2014; Mahmoudi & Mazaheri 2015); see figure 23(*d*). A triple point is also generated. A curved flame with a much lower temperature appears again (box A3), but an increased temperature is formed later when it propagates in the downstream region (box A4). Multiple triple points (box A5) and a partially smooth flame front (box A6) with lower temperature form in the leading flame tip; see figure 23(*g*,*h*). However, the combustion temperature in the downstream product is much higher than the initial overdriven detonation propagation. This is reasonable because the uniformity of the upstream mixture is much higher. Moreover, the consumption of the unburned pocket is further continued in the downstream flame through the diffusion effect and turbulent mixing generated by the K-H and R-M instabilities, as suggested by previous investigations (Austin 2003; Radulescu *et al.* 2005; Radulescu *et al.* 2007; Mahmoudi & Mazaheri 2015; Han *et al.* 2019). In general, dramatically complex dynamic behaviours of the detonation propagation, including the curved flame and cellular instability in the inhomogeneous supersonic mixture, occur.

For quantitively evaluating the detonation propagation, the flame front position at the embryonic stage and the corresponding averaged flame front propagation velocity with time evolution near the lower wall ($y/Ly = 0.1/2.0$), middle region ($y/Ly = 1.0/2.0$) and

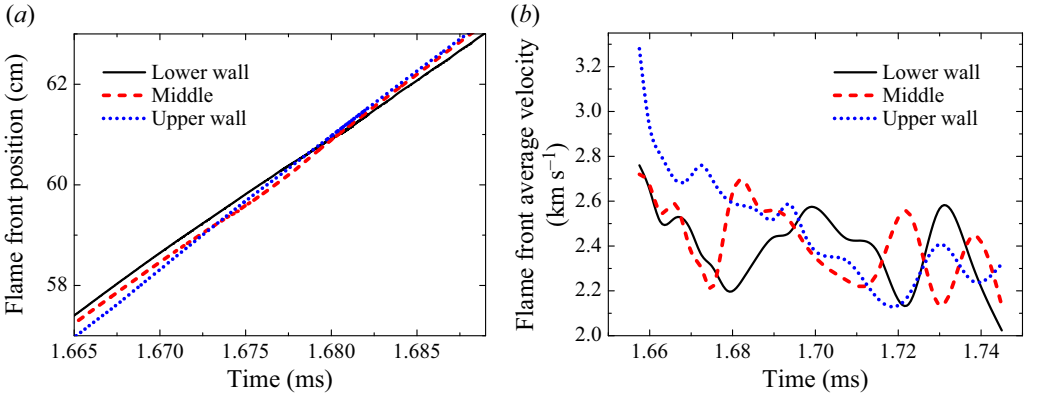

Figure 24. The (*a*) axial position of the flame front and the (*b*) corresponding averaged flame front velocity at different *y*-direction positions near the lower wall ($y/Ly = 0.1/2.0$), middle region ($y/Ly = 1.0/2.0$) and upper wall ($y/Ly = 1.9/2.0$) in case 4.

upper wall ($y/Ly = 1.9/2.0$) are plotted in figure 24(*a*,*b*), respectively. The detonation flame front first appears at the lower wall, whereas when it propagates in the upper domain and impacts the upper wall, the axial position of the flame front moves quickly, as presented in the temperature contours during the stage from $t = 1.65625$ to 1.68625 ms. However, the flame propagation in the middle region is more complicated under the influence of the fuel-lean mixture. Notably, there is a deviant velocity oscillation, especially in the lower and middle areas of the flame front. The average velocity in the upper region is gradually decreasing owing to the decrease of detonation overdriven degree. In the middle region flame, the flame propagation velocity decreases rapidly from 2700 to 2200 m s^{-1} at the developing stage but rapidly increases to 2700 m s^{-1} during the period of $t = 0.1675$–1.6825 ms and then gradually decreases to 2200 m s^{-1}. The propagation velocity in the lower region has a similar trend.

After that, a more regular oscillation of the averaged velocity occurs with high amplitude, but the average velocity in three different positions is close to 2300 m s^{-1}. Hence, the inhomogeneous mixture increases the instability of the propagation speed. In Han *et al.*'s (2019) study, a fluctuating average detonation velocity with a different amplitude was also observed in a concentration gradient with a transverse and linear distribution. They reported a much higher velocity oscillation in the fuel-rich region compared with the fuel-lean region. In the current study, an oscillation with high amplitude is also observed in the lower wall mixture, which has a high ER, but a small amplitude appears in the middle region with low ER.

Furthermore, by subtracting the flow velocity of the mixture (around 500 m s^{-1}), the detonation propagation velocity is approximately 1800 m s^{-1}. The theoretical CJ velocity for detonation propagation in the uniform mixture is 1974.95 m s^{-1}, which is calculated by Cantera when using Burke *et al.*'s (2012) chemical reaction mechanism. Consequently, there is around an 8.8 % deficit in the average propagation velocity compared with the theoretical CJ speed. This velocity deficit is consistent with previous research reported by Kessler *et al.* (2012) and Han *et al.* (2019). The flame front is, therefore, inclined remarkably under the influence of velocity deficit with different amplitudes due to the inhomogeneous mixture.

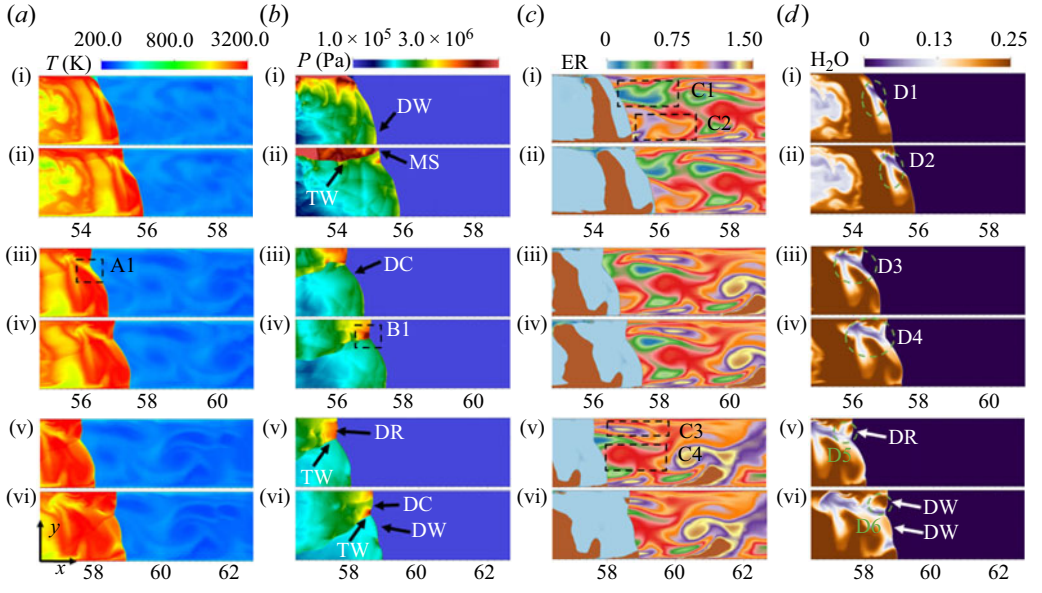

Figure 25. Snapshots of over-driven detonation propagation rendered by (first column) temperature, (second column) pressure, (third column) ER and (fourth column) product showing the decupled detonation front (case 4). DW – detonation wave, MS – Mach stem, TW – transverse wave, DC – decoupled flame, DR – detonation reinitiation: (*a*1) $t = 1.65625$, (*a*2) $t = 1.65875$, (*a*3) $t = 1.66250$, (*a*4) $t = 1.66500$, (*a*5) $t = 1.66750$ and (*a*6) $t = 1.67125$ ms.

3.4.2. *Flame front characteristics in detonation quenching and reinitiation*

To elucidate the macroscopic phenomena mentioned above, such as the curved flame front and velocity oscillation, figure 25 provides more detailed information on the flame propagation associated with the temperature, pressure, ER and combustion product during the initial time. The combustion ER map also consists of two colours, grey and brown, representing that the fuel and oxidizer are depleted, respectively, as discussed before. At $t = 1.65625$ ms, a lower ER value (0.15) exists ahead of the flame front in the upper region (box C1), but a more sensitive mixture is generated in box C2 so that there is a transverse concentration gradient. Moreover, a concentration gradient is also formed in the longitudinal direction. Hence, the ER distributions become highly complex, resulting in more propagation dynamic characteristics.

First, an intense Mach stem is formed after the overdriven detonation wave collides with the upper wall, introducing a high-pressure region and intense detonation combustion. The transverse wave is observed subsequently; see figure 25(*b*2). When the detonation wave propagates in the lower ER region, a partial flame front is decoupled with a flame and a shock wave, rapidly forming a curved flame and lower-temperature region (box A1). This is also called partial detonation quenching. The current result is in accordance with previous literature when the detonation propagates in a lower ER region from a lean to a leaner gradient. In Boulal *et al.* (2016) experimental investigation, detonation quenching occurs in an inhomogeneous mixture with a lean-to-leaner distribution. In their research, a reduced number of transverse waves is observed and even the detonation quenching occurs in the fuel-lean mixture, where the ER value is around 0.2. Hence, this value is close to the current research. It is noted that the detonation quenching does not mean combustion extinction. A detonation reinitiation occurs later. As reported by Zheng *et al.*'s (2019) study, the detonation wave was rapidly decoupled into a shock and a flame when the

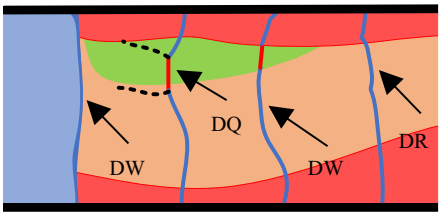

Figure 26. Physical illustration of the curved detonation wave, partially decoupled detonation and detonation re-initiation. DW – detonation wave, DQ – detonation quenching, DR – detonation reinitiation.

flame front travelled through an extremely inhomogeneous mixture. Han *et al.* (2019) also numerically reported the decoupled flame front. They suggested the LSW is decoupled from the chemical reaction layer due to the quite fuel-lean mixture with a lower OH mass fraction. However, in their works, the inhomogeneous mixture has a linear transverse concentration gradient. A more complicated mixture is not considered.

In the current decoupled detonation flame front associated with partial detonation quenching, an accumulation of increased pressure is yielded in this front, as presented by box B1 in figure 25(*b*4). When the intense shock wave propagates into these regions with a higher ER value (boxes C3 and C4), the detonation reinitiation is triggered in the partially flame front; see figure 25(*b*5). The detonation reinitiation was also reported in the previous experimental study, where the detonation decay could reinitiate in the non-uniform mixture with 14.0 %–19.0 % hydrogen (Kuznetsov *et al.* 1998). This value is close to the current result. Then, a more uniform flame front is observed since the flame front propagates in a region having high and uniform ER regions. Such a result also contributes to an uneven distribution of the combustion product of H_2O, and a gradually increasing penetration region with a lower H_2O mass fraction is generated, as shown in circles D1–D4. Accompanying the formation of detonation reinitiation, a high mass fraction of H_2O is yielded again in the flame front; see circles D5 and D6. Therefore, the complicated dynamic characteristics, including the curved flame front, partially decoupled flame front and detonation reinitiation, are combined results in the high and low sensitive mixtures along the parallel and transverse directions and transverse wave.

Figure 26 depicts a schematic representation detailing the intricate evolution of detonation wave bending, quenching and subsequent reinitiation. Here, the blue region signifies combustion products, while the blue line traces the path of the detonation wave. Additionally, the red, green and yellow areas correspond to high, low and optimal ERs, respectively. When the detonation wave advances into the low ER region, the combustion expansion fails to sustain a self-sustaining detonation, owing to fuel scarcity. Consequently, this results in partial bending and decoupling of the detonation wave front. However, upon traversing into the optimal ER region represented by yellow, the detonation wave reignites, thereby restoring its flat-fronted propagation.

To draw the influence of an inhomogeneous mixture on the detonation propagation speed, figure 27 gives the instantaneous flame propagation velocity near the (red line) lower and (blue line) upper walls at different periods, corresponding to figure 25(*a*2,*a*3), respectively. All flame front propagation velocities have a high oscillation within 1750–3500 m s^{-1} due to the inherent unstable feature of the detonation wave (Austin 2003). A rather higher amplitude of the flame propagation velocity in the upper wall is formed compared with the lower flame propagation velocity. This contributes to the intense Mach stem, which increases the intensity of the detonation wave.

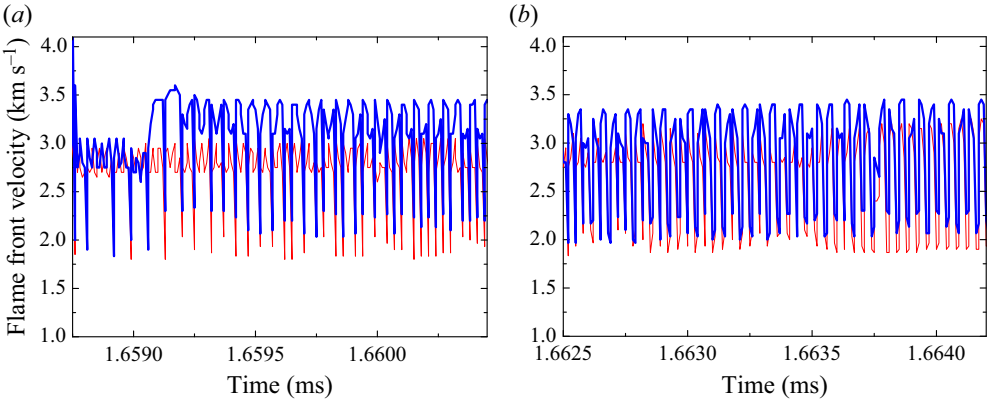

Figure 27. Transient detonation propagation velocity near (red curve) lower wall ($y/Ly = 0.1/2.0$) and (blue curve) upper wall ($y/Ly = 1.9/2.0$) in case 4 at different periods (*a*) $t = 1.65875$–1.66045 ms, (*b*) $t = 1.6625$–1.6642 ms.

3.4.3. *Detonation front structure and instability*

To compare the differences between the decoupled flame and detonation wave at $t = 1.6625$ ms, the flame front structure is superimposed in figure 28(*c*,*d*), and for lines B ($y/Ly = 1.4/2.0$) and C ($y/Ly = 1.9/2.0$) in figure 28(*a*). A very fuel-lean mixture is formed with a value of $H_2 = 0.007$. After the shock wave, the H, O and OH increase rapidly, followed by HO_2 and H_2O_2 radicals, while the peak values of H and O radicals are pretty small at $H = 0.00033$ and $O = 0.0122$. Subsequently, with the consumption of H_2 and HO_2, less energy release is formed, resulting in a lower increased temperature from 1054 to 1430 K. Hence, the main contribution of the increasing temperature is formed by the decoupled LSW. To thoroughly analyse the connection between the decoupled flame front's shock wave and flame structure, figure 29 gives the temperature, pressure and OH variations along line B. As demonstrated, after the intense post-shock period, the temperature of the fresh mixture is increased rapidly; then a lower increasing ratio appears within the chemical reaction. Here, a rather lower peak mass fraction of $OH = 0.0056$ appears. Moreover, the distance between the LSW and the reaction front is around 0.4 mm so that the LSW is decoupled from the reaction layer due to the extreme fuel-lean mixture. As a result, the simulation of the extreme fuel-lean and fuel-rich mixtures needs a detailed hydrogen–air chemistry reaction mechanism because of the complex dynamic behaviours, especially for the detonation quenching and partially decoupled flame front.

In addition to the detonation front structure along line C in figure 28(*d*), thanks to the intense shock wave, a rapid increase of mass fraction appears in the O and H radicals, followed by HO_2 and H_2O_2. The peak values of H, O and OH reach 0.00264, 0.04376 and 0.0206, respectively, much higher than the deflagration flame, as discussed in the premixed mixture, especially in the OH radical. Moreover, compared with the deflagration flame, the H and O radicals appear early in the flame front instead of the HO_2 and H_2O_2. As such, the flame front structure is significantly different due to the early LSW. Moreover, the peak value of HO_2 approaches 4.5×10^{-5} through the chain-breaching reaction of $H + O_2(+M) = HO_2(+M)$, which is almost two times that of the deflagration flame front. This is due to the HO_2 radical being associated with pressure, which is more vital for the detonation flame with high pressure. After that, with the abrupt consumption of HO_2 and H_2O_2, the mass fraction of OH and H_2O radicals is increased accordingly with the main chain-branching reactions through $HO_2 + H = OH + OH$ and $HO_2 + OH = H_2O + O_2$,

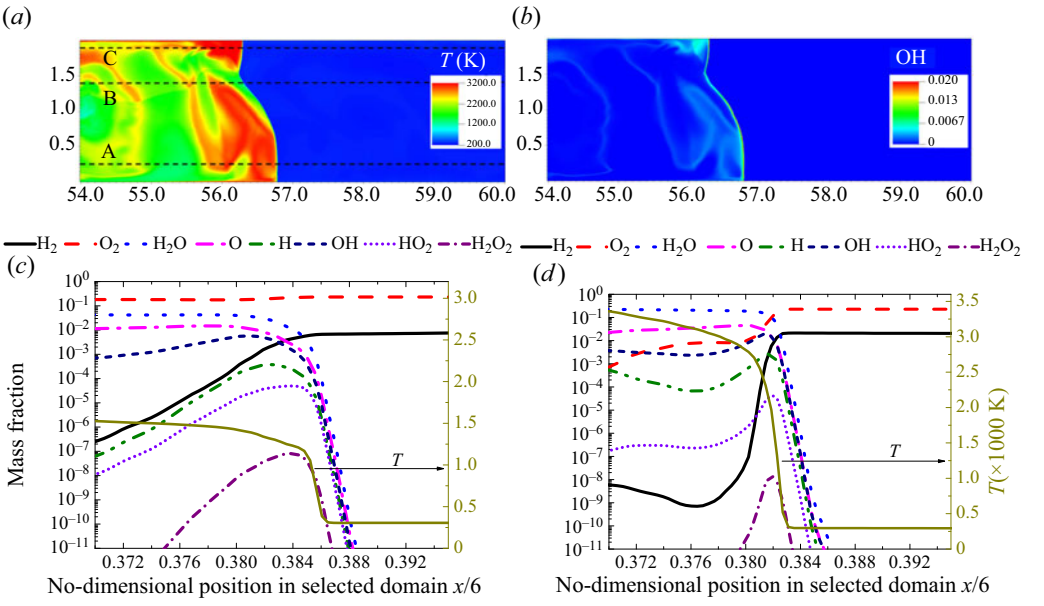

Figure 28. The (*a*) temperature contour, (*b*) OH contour, and the corresponding mass fraction of the flame front structure near the (*c*) decoupled detonation flame (line B, $y/Ly = 1.4/2.0$) and (*d*) upper wall (line C, $y/Ly = 1.9/2.0$) at $t = 1.6625$ ms in case 4.

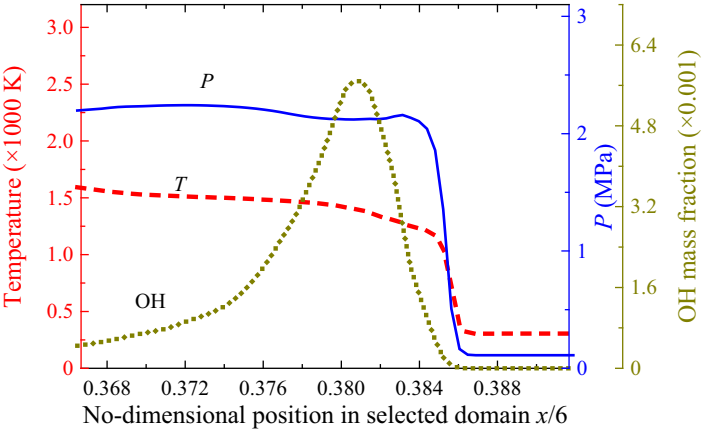

Figure 29. The temperature, pressure and OH variations along line B for the decoupled detonation front at t = 1.6625 ms (see figure 28*a*).

resulting in a high energy release ratio, and feeding back to a dramatic increase in temperature that reaches 3200 K.

Furthermore, we analysed the local detonation combustion and product. The profiles of the mass fraction of H_2 and the local *Ma* number along lines A, B and C at $t = 1.6625$ ms are given in figure 30(*a*,*b*), respectively. Residual hydrogen exists in the downstream flame; see circles A and B, especially in line A, and the H_2 mass fraction reaches 0.012, implying that the H_2 is not consumed fully behind the detonation front. Several previous studies have also found these results in homogenous and inhomogeneous mixtures (Austin 2003; Radulescu *et al.* 2005, 2007; Mahmoudi & Mazaheri 2015; Han *et al.* 2019). Subbotin (1975) and Gamezo, Desbordes & Oran (1999) suggested that the unburned material

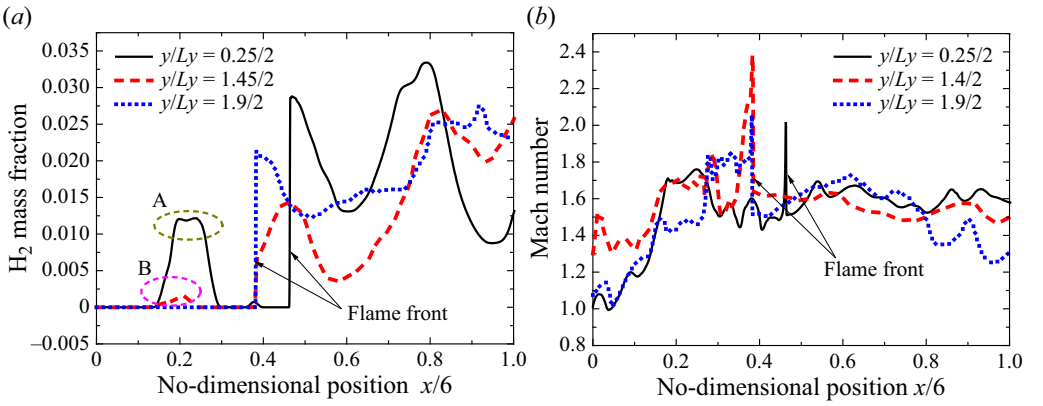

Figure 30. Variations of macroscopic variables of (*a*) H_2 and (*b*) Mach number along lines A, B and C in figure 28(*a*).

is highly related to the detonation instability, and the unburned material appears in a highly unstable detonation propagation. In Sharpe's (2001) work, they reported that the formation of an unburned material is generated by the departure of the slip line and secondary triple point. Mahmoudi & Mazaheri (2015) also found an unreacted mixture when using a high mesh resolution simulation considering the viscosity. More recently, the unburned material was observed in an inhomogeneous mixture (Han *et al.* 2019), and Han *et al.* (2019) revealed that more unburned pockets after the detonation front are generated when steepening the mixture concentration gradient. In the present research, due to the concentration gradient in both the longitudinal and horizontal directions, the residual hydrogen appears more random and mainly depends on the ER value. At $t = 1.6625$ ms, the ER value is much higher ahead of the lower detonation front, as noted in figure 25(*c*2) near the bottom wall. As a result, a high bulk of residual hydrogen occurs when the denotation wave propagates in these regions.

By insight into the Mach number profile, the average Mach number ahead of the flame front is close to 1.5. A steep increase in Mach number is due to the LSW. After the combustion process, the pressure expands with a decrease in pressure and density. Regarding the Mach number, the ideal ZND solution quickly approaches the local speed of sound, namely, $Ma = 1$, while in the current inhomogeneous supersonic mixture, it needs more time to reach the sonic point. Such a feature is attributed to the intense flow instabilities generated by the non-equilibrium chemical reaction in the downstream chamber, where a continuous reaction of the unburned pocket appears under the influences of the R-M and K-H instabilities. In Radulescu *et al.*'s (2007) study, the delayed equilibrium reaction was also reported when comparing the detonation structure and the variations of the sonic surface. By employing the same method, Han *et al.* (2019) also found that the non-equilibrium reaction is elongated when steeping the concentration gradient. Hence, the present result is qualitatively consistent with the previous study.

To reveal the detonation instability, figure 31 gives the next detonation propagation scenarios from $x = 66$ to $x = 73$ cm, accompanied by the pressure, ER and combustion product of H_2O. First, a curved flame with a lower temperature appears due to the fuel-lean mixture (box C1 in figure 31*c*1), while a detonation reinitiation is observed when this flame front propagates into a high ER mixture. A remarkable triple point is generated and propagates from the lower wall to the upper wall (circles A1–A3). At $t = 1.715$ ms, a complicated flame front is generated. A detonation wave is decoupled again (see DC2 in

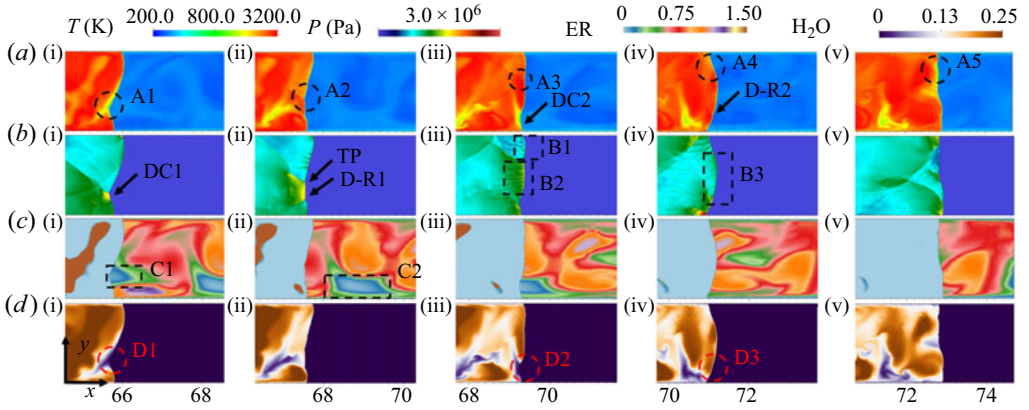

Figure 31. Snapshots of detonation propagation rendered by (first row) temperature, (second row) pressure, (third row) ER and (fourth row) product showing the partially decupled detonation front and irregular detonation cellular structure in case 4. DC – decoupled flame, TP – triple point, D-R – detonation re-initiation: (*a*1) $t = 1.7$, (*a*2) $t = 1.7075$, (*a*3) $t = 1.715$, (*a*4) $t = 1.7225$ and (*a*5) $t = 1.7300$ ms.

figure 31*a*3) to a flame and a shock wave since it propagates in the lower ER region (circle C2), followed by a lower combustion product (circle D2), while a multiple-head detonation wave is generated in the upper flame front; see boxes B1 and B2. Yet, the cell distribution is irregular, and therefore, an irregular detonation wave is formed. At $t = 1.7225$ ms, the detonation wave propagates downstream, detonation reinitiation in circle D3 and a smooth flame front with a large detonation cellular size are observed (box B3). As a result, the inhomogeneous promotes the detonation instability with an irregular wave. As the flame front travels into the fuel-lean mixture, an increasing induced reaction zone forms in circle A5.

Figures 32 and 33 further provide detailed detonation wave structures and corresponding density schlieren enlargements for part of the time in figure 31. When the decoupled shock propagates to an appropriate ER area, detonation reinitiation occurs, and part of the detonation wave appears in a low-temperature area downstream of combustion, as shown in the green area in figure 32(*a*). At the same time, the structure of the detonation wave is complex. The theoretical detonation cell size in the premixed mixture is around 9.0 mm when using the Cantera tool calculation. However, an irregular detonation propagation is generated in the computational domain, where the detonation cell size is small in the upper domain. In comparison, the detonation cell size in the lower half-domain is quite large. This is mainly due to a large transverse concentration gradient in the mixture. In general, the detonation cell size is small compared with the theoretical size. The numerical results of the previous study (Hu *et al.* 2005) also obtained a relatively smaller cell size than the experiment, which is explained by the higher heat loss at the wall in the experiment (Fickett & Davis 2000). Due to the use of adiabatic wall BCs and the limitations of 2-D simulation, it is still reasonable to obtain a small cell size in the numerical simulation.

The temperature distribution of the detonation wave is uneven, and the temperature in the lower half-domain is relatively high. This is mainly because the ER distribution in the longitudinal direction is particularly uneven, leading to different triple point structure distributions and an uneven temperature distribution. The density schlieren in figure 32(*b*) shows that multiple transverse waves are generated in a smaller range downstream of the detonation front. In contrast, high-intensity transverse waves extend to a long area downstream in the entire combustion chamber.

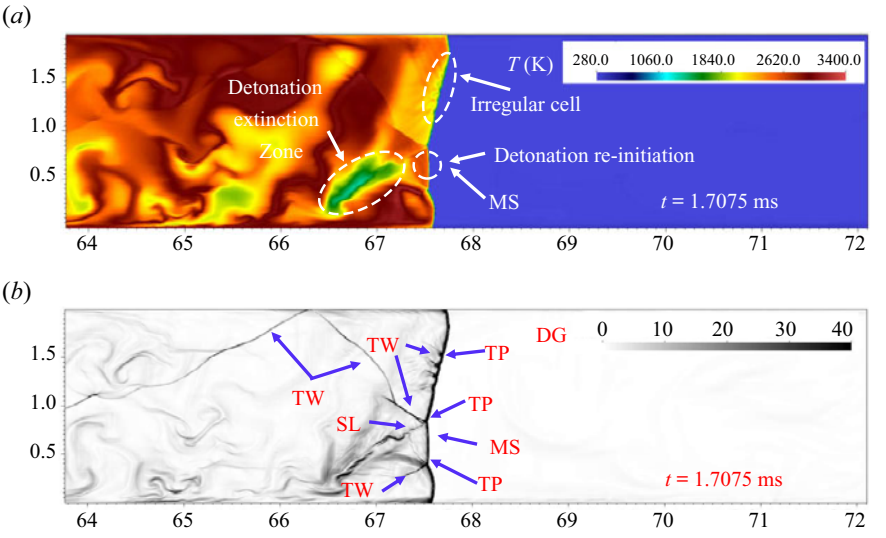

Figure 32. Flame front structure and detonation propagation instability in inhomogeneous supersonic mixture rendered by temperature contour (*a*) and destiny schlieren (*b*) at $t = 1.7075$ ms. TW – transverse wave, TP – triple point, SL – slipping line, MS – Mach stem.

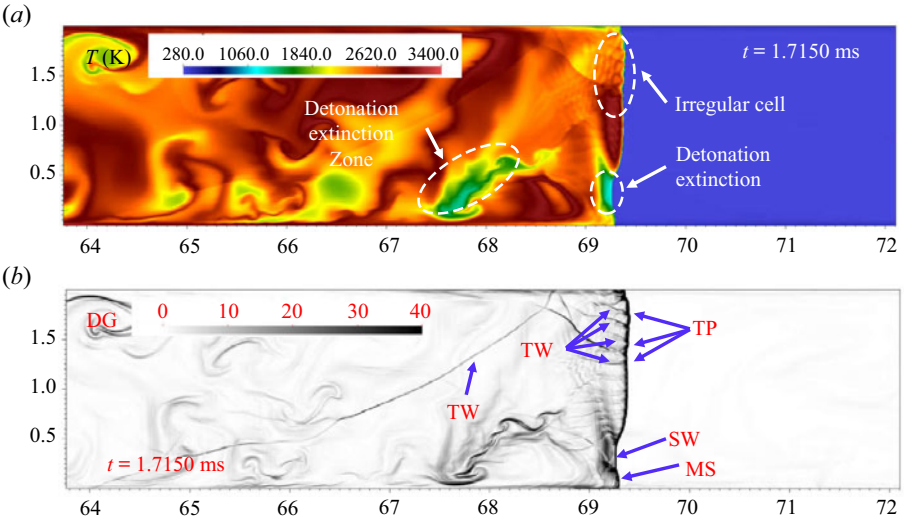

Figure 33. Flame front structure and partial decouple flame front rendered by temperature contour (*a*) and destiny schlieren (*b*) at $t = 1.7150$ ms. TW – transverse wave, TP – triple point, SW – shock wave, MS – Mach stem.

Figure 33 further shows the detonation extinction and complexity of the detonation wave structure. At this moment, part of the detonation wave is extinguished due to a lack of fuel near the lower wall, resulting in a low-temperature area on the flame front and downstream. But the decoupled shock wave still propagates forward. Meanwhile, multiple triple points and many transverse waves are generated in the upper part. In contrast, the stronger transverse waves in the combustion products still propagate up and down in the combustion chamber. It can, therefore, be concluded from these two moments that, in

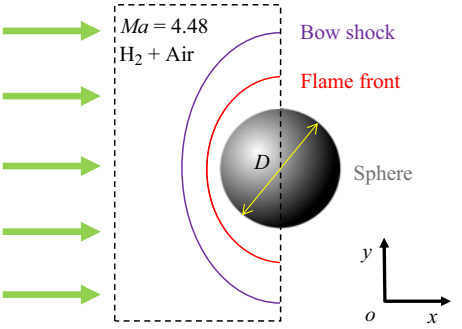

Figure 34. Physical illustration of the Leher's shock-indued oscillation combustion.

an inhomogeneous supersonic mixture, the instability and complexity of detonation wave propagation are formed due to inhomogeneous ER distribution.

4. Conclusions

In the current research, the mixing, FA and DDT in premixed and inhomogeneous supersonic mixtures are investigated comprehensively by using the N-S equations with high mesh resolution of the AMR technique and a detailed chemical reaction mechanism of 11 species and 27 steps. Of interest, the inhomogeneous mixture is generated by considering the mixing process extracted from an air-breathing detonation engine. The transverse jet obstacles are employed to trigger the DDT after mixture ignition. Comparisons of the FA between premixed and inhomogeneous mixtures are discussed. The DDT, detonation quenching, reinitiation and propagation in the inhomogeneous mixture are comprehensively reported and analysed.

- It is challenging to undergo a DDT in premixed and inhomogeneous mixtures in a smooth tube without a particular turbulent generation, even when in a supersonic flow state before mixture ignition. With the stimulation of multiple head-on transverse jet obstacles, the DDT occurs against the boundary wall due to the auto-ignited flame kernel after the intense LSW in the premixed mixture.
- The combustion temperature in the inhomogeneous mixture without jet obstacles is extremely lower in contrast to the premixed mixture due to the quite fuel-rich and fuel-lean mixtures. However, an increasing temperature is observed in the downstream flame thanks to the further turbulent mixing combustion. Additionally, the flame thickness in the inhomogeneous mixture is much higher than that of the premixed mixture. The front structure is also more complicated with further downstream non-equilibrium chemical reaction attributed to the further turbulent mixing process in contrast to the premixed mixture.
- In the inhomogeneous supersonic mixture, the onset of detonation and detonation reinitiation are formed, and both DDT mechanisms are ascribed to the robust Mach stem with the Zel'dovich gradient mechanism. The detonation extinction is caused by the vast bulk of lower ER regions. Still, the detonation reinitiation can occur and survive successfully even under a rather small, elongated highly sensitive mixture. The extreme fuel-lean mixture (ER = 0.15) results in a partially decoupled flame front, but detonation reinitiation occurs when the shock wave propagates in a highly sensitive mixture.

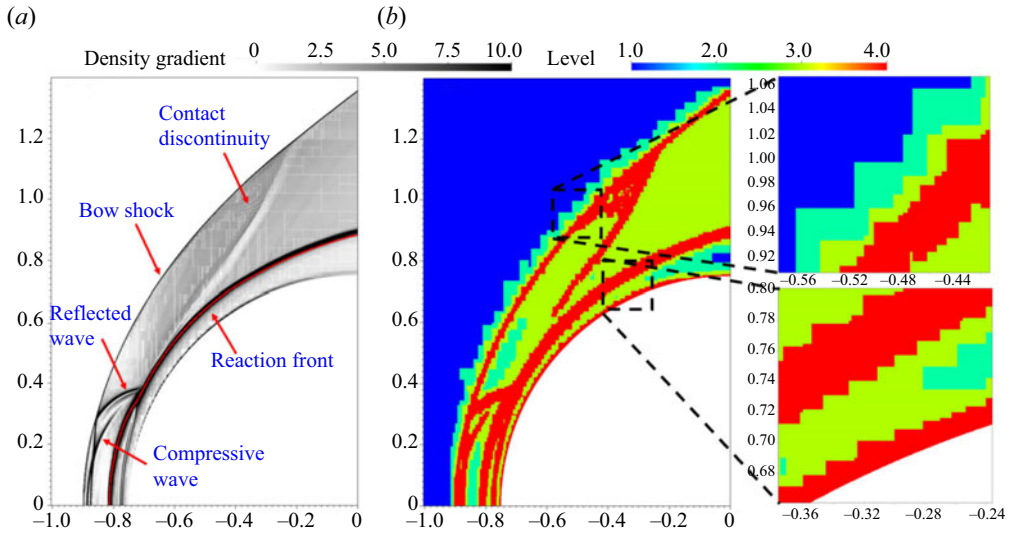

Figure 35. Flow structure identified by (*a*) density gradient and the corresponding (*b*) AMR distribution.

- The formation of detonation reinitiation requires a highly sensitive mixture region so that a discretized low ER mixture can be utilized to block the detonation propagation. However, the detonation reinitiation can be activated later when the intense shock wave propagates in a highly sensitive mixture.
- The discrete and random inhomogeneous mixture with transverse and longitudinal concentration gradients results in a curved and partially decoupled flame front. Moreover, the extreme inhomogeneous mixture increases the instabilities of the propagation speed and cellular detonation structure, reduces the averaged detonation propagation speed and delays the sonic point thanks to the extended non-equilibrium reaction.

In the current study, 2-D simulations are employed. Although, as reported by former research (Gamezo *et al.* 2007; Goodwin *et al.* 2016; Xiao & Oran 2020), the DDT mechanisms between 2-D and 3-D simulations are almost the same, the mixing process, *Br* and diffusion effect between two and three dimensions are still different. Therefore, further investigation into 3-D simulations, closer to practical detonation-based engines, is warranted. Additionally, while the current mesh resolution is adequate for resolving FA and DDT, higher resolution is required for accurately capturing detonation propagation, especially irregular detonation propagation. Nonetheless, the current study still yields significant qualitative insights into detonation simulation, particularly in engineering applications featuring extremely long combustion chambers.

Funding. This work was supported by the National Natural Science Foundation of China (nos. 11925207, 11702323 and 91741205), the China Scholarship Council (no. 202106110005), the Natural Science Foundation of Hunan Province (nos. 2024JJ6454, 2023JJ10048) and the Youth Independent Innovation Science Foundation of National University of Defense Technology (no. ZK24-34).

Declaration of interests. The authors report no conflict of interest.

Author ORCIDs.
Wandong Zhao https://orcid.org/0000-0002-6382-7596;
Xiaodong Cai https://orcid.org/0000-0001-5308-0882;
Mingbo Sun https://orcid.org/0000-0003-1676-4008.

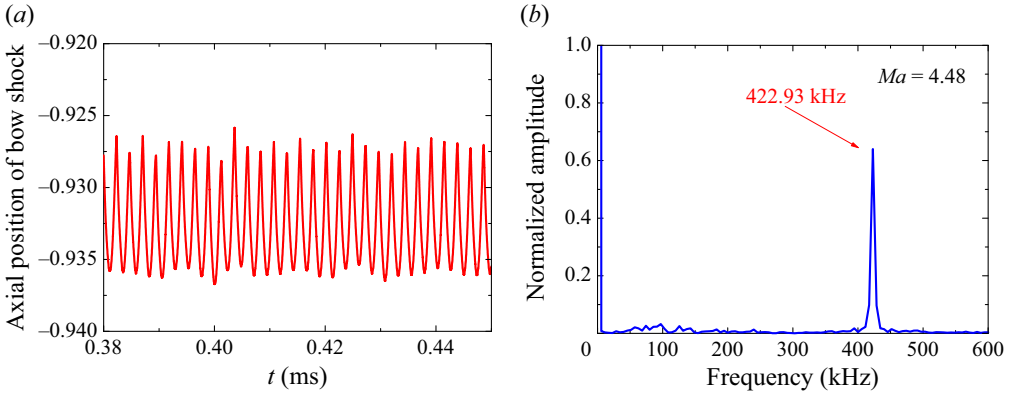

Figure 36. The axial position of bow shock wave versus time and the fast Fourier transfer data under supersonic flow of $Ma = 4.48$.

Indicator	H	H_2	O_2	O	H_2O	OH
$S_Y(\times E-2)$	0.2	1.2	10	1	8.5	1.3
$\eta_Y(\times E-4)$	50	20	20	50	10	50

Table 4. The AMR indicator parameters for shock-induced combustion.

Appendix A. Shock-induced combustion

To test the numerical model and AMR technique to resolve the compressible flow and detonation combustion, the shock-induced combustion and FA test cases are carried out. Meanwhile, the obtained results are also compared with experimental data.

First, a classical shock-induced combustion conducted by Lehr is selected (Lehr 1972). The physical model is given in figure 34. The radius of the supersonic projectile is 7.5 mm. A half-computational domain of $L_x \times L_y = 12$ mm $\times$ 18 mm is utilized to reduce computing resources. The cylinder symmetry is considered in a splitting approach. The incoming hydrogen–air mixture with Mach number 4.48 flows into the domain with a velocity inlet on the left side of the computational domain. The remaining three directions of the computational domain have an outflow BC. The incoming pressure and temperature are 0.42 atm and 293 K, respectively.

Of note, here, the AMR threshold selection is also introduced. The selection mainly depends on two refinement criteria. The first AMR criterion is to estimate the surrounding cells' differences between the arbitrary scalar, which is employed for the large gradient regions such as the shock and detonation waves. The second AMR criterion is to evaluate the local truncation error by Richardson extrapolation. For the temperature, density and pressure variables, the first AMR criterion is used, and the scaled gradient thresholds are set as $\varepsilon_T = 500$ K, $\varepsilon_\rho = 0.020$ kg m^{-3}, $\varepsilon_P = 8E4$ Pa, respectively. The second AMR criterion is adopted for all species. All AMR thresholds are listed in table 4, where S_Y and η_Y are scaling parameters for relative errors and absolute errors, and the detailed definition can be found in Deiterding (2011). A hydrogen–air chemical reaction mechanism with 9 species and 19 steps proposed by Jachimowski (1988) is employed. An initial mesh is 160×240. Four AMR levels with (2, 2, 4) are adopted, generating a minim size of 0.0046875 mm.

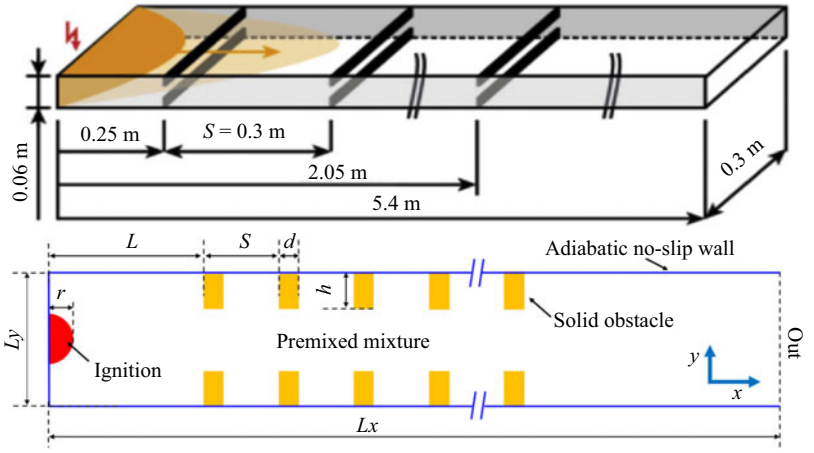

Figure 37. Physical illustration of (*a*, upper row) experimental configuration from Ettner *et al.* (2013) and (*b*, lower row) reduced 2-D simulation model.

Figure 35 exhibits the density gradient contour and the corresponding AMR distribution. It is observed that the AMR works well practically in its adept handling of the shock and reaction front. Besides that, the AMR has still refined the compressive wave. Hence, it can be inferred that the AMR threshold is efficient under the current setting parameter. The axial position of the bow shock wave versus time and fast Fourier transform for the shock's position are plotted in figures 36(*a*) and 36(*b*), respectively. A periodic oscillation of the bow shock is formed, and the obtained oscillation frequency is 422.93 kHz, as depicted in figure 36(*b*). The oscillation frequency obtained by Lehr's experimental data is 425 kHz. Hence, there is just a 0.48 % deviation. It is concluded that the Roe–HLL solver is accurate in addressing the complex inherent in supersonic reactive combustion.

Appendix B. Flame acceleration and DDT test

Second, the FA and DDT are simulated and compared with previous experimental and numerical data. The computational configuration is extracted from Ettner's experimental set-up (Azadboni *et al.* 2017) as demonstrated in figures 37(*a*) and 37(*b*). Thanks to the symmetry structure, the 3-D rectangular configuration can be reduced to a 2-D set-up, but the blockage ratio, solid obstacle's interval and tube width are kept the same. The specific parameters can be found in figure 37(*b*). To reduce the computational requirements, the combustion chamber length is reduced to 3.6 m. The simulation configuration has 0.6 *Br* and a 0.3 mole fraction of hydrogen in a homogeneous state. More detailed configuration parameters can be found in Wang & Wen (2017) and Azadboni *et al.* (2017).

The initial mesh size is set to be $L_x \times L_y = 9000 \times 360$. Four AMR levels are adopted with $r_1 = 2$, $r_2 = 2$ and $r_3 = 4$. It is noted that the first AMR criterion is used for the temperature, density and pressure with $\varepsilon_T = 500$ K, $\varepsilon_\rho = 0.01$ kg m^{-3}, $\varepsilon_P = 4E4$ Pa, while the second criterion is employed for key species, and the corresponding AMR thresholds are listed in table 5. Meanwhile, Burke *et al.*'s chemical reaction mechanism is employed for the current FA and DDT, which has been widely used for DDT simulation, as discussed before.

A weak hot spot with a temperature of 2500 K and a pressure of 0.1 MPa located in the centre of the left side of the computational domain is used for mixture ignition.

Indicator	H	H_2	O_2	O	H_2O	OH
$S_Y(\times E-2)$	0.2	1.0	10	1	8.5	1.0
$\eta_Y(\times E-4)$	50	35	30	50	10	50

Table 5. The AMR indicators for the key species in FA simulation.

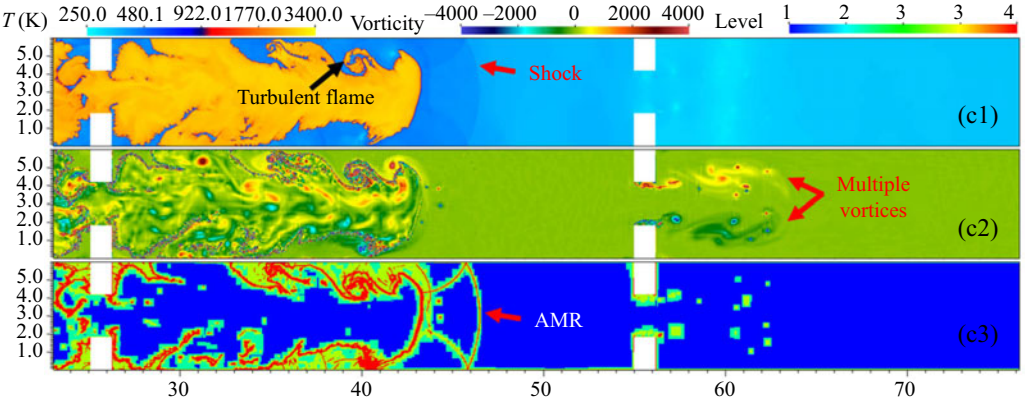

Figure 38. Temperature, vorticity and AMR distribution transient contours in FA.

The transient FA temperature, vorticity and AMR distribution contours are presented in figure 38. As shown, the highest AMR level covers the large density gradient region for shock waves, flame front and boundary walls. As a result, the AMR thresholds are efficient.

The obtained flame propagation velocity and the previous literature's results are superimposed in figure 39. As such, the flame front propagation velocity obtained by the current solver is almost the same as the reference value. It is worth mentioning that the large velocity oscillation in the experimental data is due to the flame front position obtained in different monitors at different times. Further, detonation propagation is obtained after a distance of 1.6 m for the current numerical and previous literature data. Referring to the CJ velocity, the differences from the ideal value are 1.23 %, 5.18 %, 3.74 % and 0.13 % for the experiment of Ettner (2013), Wang & Wen's (2017), Zhao *et al.*'s (2022*b*) and the current simulation data, respectively. Therefore, the present AMR and Roe solver are robust and reliable for 2-D FA and DDT scenarios.

Appendix C. Difference of flame acceleration and DDT between 2-D and 3-D cases

To analyse the 2-D and 3-D differences in FA and DDT, we further carried out a 3-D simulation in the supersonic premixed mixture considering the multiple transverse jet obstacles in a rectangular combustion chamber. The incoming temperature, pressure and species are consistent with case 2, as listed in table 2. Multiple transverse jets are injected into the chamber during the FA stage, as illustrated by the dashed blue curve in figure 40. In order to reduce the computing effort, the physical domain size is set to be 450.00 mm, 15.12 mm and 15.12 mm in z-, x- and y-directions, respectively. The hot spot ignitions are also located in the upper and lower walls. The initial mesh is set to be $L_x \times L_y \times L_z = 1250 \times 42 \times 42$ cells, generating an identical size of $\mathrm{d}x = \mathrm{d}y = \mathrm{d}z =$ 0.36 mm. Three AMR levels with $r_1 = 2$ and $r_2 = 4$ are utilized in the whole simulation to

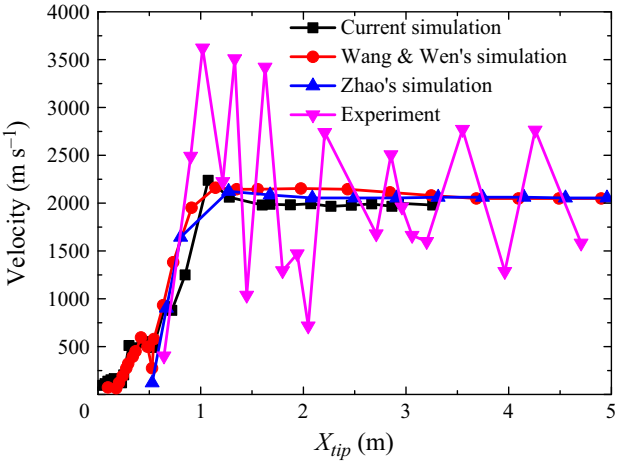

Figure 39. The obtained flame tip propagation velocity versus flame position for the current simulation and previous literature data.

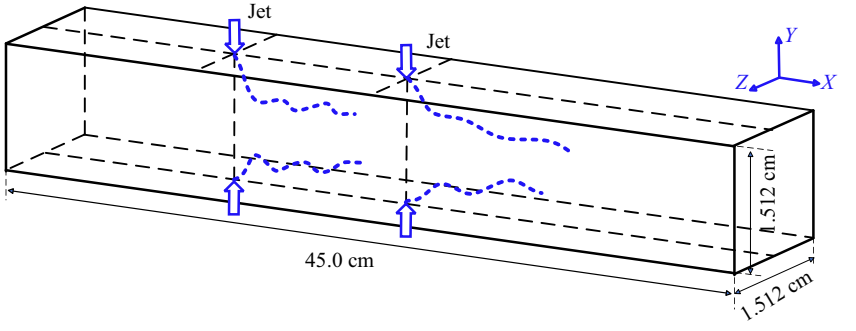

Figure 40. Physical illustration of FA and DDT in 3-D rectangle with transverse jet.

reduce the computing cost. The corresponding AMR minimum mesh size is 0.045 mm so that around 1.1289 billion mesh will be generated if a uniform mesh is adopted.

Figure 41 shows the temperature iso-surface evolution during FA and DDT processes under a supersonic uniform mixture. It can be seen from the figure that the flame surface gradually appears as a bifurcated flame front structure (bifurcated flame front) under the influence of the transverse jet in the y-direction. Under the influence of the disturbance flow field of transverse jet obstacles, the flame surface area increases, and the flame propagation speed increases. Immediately afterward, a spherical local explosion point appears on the lower left wall in figure 41(e), which in turn leads to a rapid increase in the local combustion temperature. The localized explosion point quickly evolves into a smooth detonation combustion wave s at 0.38–0.4 ms and propagates further downstream. Therefore, the results of shock waves, certain blockage effects and flow disturbance effects generated by 3-D transverse jets in the flow field are consistent with those of 2-D transverse jets.

Figure 42 shows the local temperature enlargement contours before and after the detonation occurs at the middle plane of the z-axis. As presented, the flame front structure is complex, and many wrinkled flames are generated. When the LSW collides and converges with multiple rear shock waves, a local detonation point appears on the upper

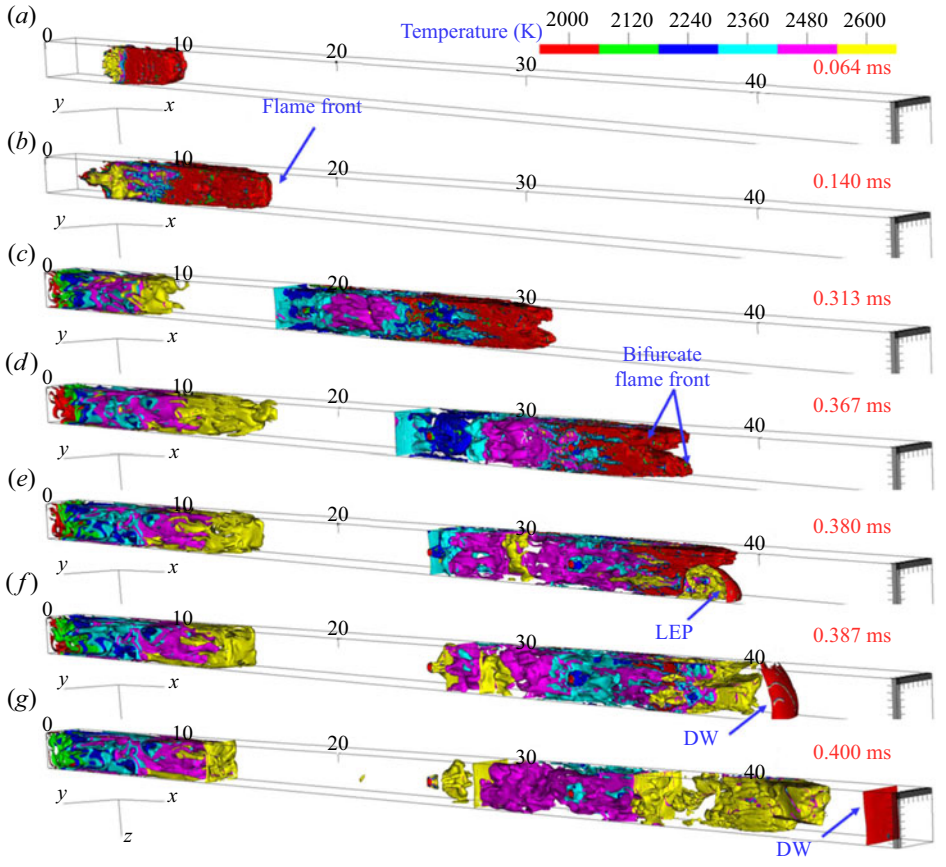

Figure 41. Evolution of temperature iso-surface in FA and DDT in the supersonic premixed mixture. LEP – localized explosion point, DW – detonation wave.

wall in front of the flame front, and this explosion point further evolves into a detonation wave.

Therefore, the detonation of DDT in a 3-D supersonic homogeneous mixture mainly relies on the high-pressure explosion point formed by the convergence of multiple shock waves on the upper wall and eventually evolves into a detonation wave. This detonation mechanism is the same as the 2-D case. It can be concluded that, in a supersonic homogeneous mixture, the 2-D and 3-D detonation mechanisms are basically consistent with one another, which further verifies the feasibility of 2-D simulation in revealing the DDT mechanism.

In summary, the numerical model can be extended to carry out 3-D FA and DDT simulations. Prior studies reported that 2-D numerical simulation can also reproduce the flame evolution, flame–shock interaction, shock–shock interaction, DDT and detonation propagation characteristics as provided in 3-D simulation and experimental study (Xiao & Oran 2019). A lot of the former literature related to the FA and DDT confirmed that 2-D simulation is in qualitative and quite quantitative agreement with the obtained results in 3-D numerical simulation and experimental studies. Numerous works have reported that the DDT mechanism between two and three dimensions is almost the same (Gamezo *et al.* 2007; Ogawa *et al.* 2013; Goodwin *et al.* 2016; Xiao & Oran 2020). The reason is

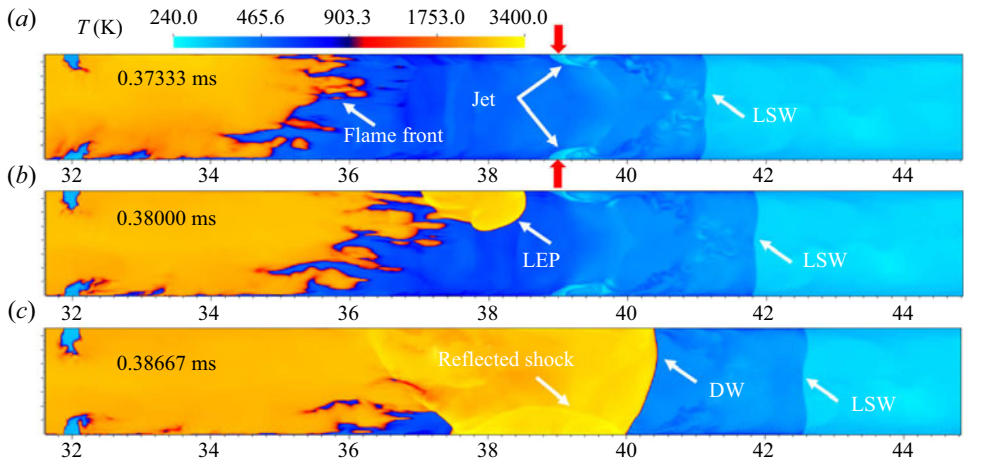

Figure 42. Snapshot of temperature contour before and after DDT in the z-direction. LSW – leading shock wave, LEP – localized explosion point, DW – detonation wave.

that the DDT evolution is mainly controlled by shock–shock and shock–flame interactions. Moreover, the growth rate in the R-M instability introduced by the shock–flame interaction between two and three dimensions is the same and has a linear regime (Li & Zhang 1997). The difference is that the growth rate in the 3-D case is slightly faster than in the 2-D results. As such, the DDT mechanisms between the two and three dimensions are the same despite the fact that there is some difference in the flame propagation speed (Ogawa *et al.* 2013). The current 3-D simulation also confirmed the same DDT mechanism. However, the 2-D model still has some limitations in reproducing some 3-D flow and detonation structures, such as the turbulent flow and detonation propagation structure.

References

Ahmed, K.A. & Forliti, D.J. 2009 Fluidic flame stabilization in a planar combustor using a transverse slot jet. *AIAA J.* **47** (11), 2770–2775.

Austin, J.M. 2003 The role of instability in gaseous detonation. PhD thesis, California Institute of Technology.

Azadboni, R.K., Heidari, A., Boeck, L.R. & Wen, J.X. 2019 The effect of concentration gradients on deflagration-to-detonation transition in a rectangular channel with and without obstructions – a numerical study. *Intl J. Hydrogen Energy* **44** (13), 7032–7040.

Azadboni, R.K., Wen, J.X., Heidari, A. & Wang, C. 2017 Numerical modeling of deflagration to detonation transition in inhomogeneous hydrogen/air mixtures. *J. Loss Prev. Process. Ind.* **49**, 722–730.

Bird, R.B., Stewart, W.E. & Lightfoot, E.N. 2006 *Transport Phenomena*. John Wiley & Sons.

Boeck, L.R., Berger, F.M., Hasslberger, J. & Sattelmayer, T. 2016 Detonation propagation in hydrogen–air mixtures with transverse concentration gradients. *Shock Waves* **26** (2), 181–192.

Boeck, L.R., Hasslberger, J. & Sattelmayer, T. 2014 Flame acceleration in hydrogen/air mixtures with concentration gradients. *Combust. Sci. Technol.* **186** (10–11), 1650–1661.

Boivin, P., Jiménez, C., Sánchez, A.L. & Williams, F.A. 2011 An explicit reduced mechanism for H2–air combustion. *Proc. Combust. Inst.* **33** (1), 517–523.

Boulal, S., Vidal, P. & Zitoun, R. 2016 Experimental investigation of detonation quenching in non-uniform compositions. *Combust. Flame* **172**, 222–233.

Burke, M., Chaos, M., Ju, Y., Dryer, F. & Klippenstein, S. 2012 Comprehensive H2/O2 kinetic model for high-pressure combustion. *Intl J. Chem. Kinet.* **44** (7), 444–474.

Cai, X., Deiterding, R., Liang, J. & Mahmoudi, Y. 2017 Adaptive simulations of viscous detonations initiated by a hot jet using a high-order hybrid WENO–CD scheme. *Proc. Combust. Inst.* **36** (2), 2725–2733.

CAI, X., LIANG, J., DEITERDING, R., MAHMOUDI LARIMI, Y. & SUN, M.-B. 2018 Experimental and numerical investigations on propagating modes of detonations: detonation wave/boundary layer interaction. *Combust. Flame* **190**, 201–215.

CHENG, J., ZHANG, B., LIU, H. & WANG, F. 2020 Experimental study on the effects of different fluidic jets on the acceleration of deflagration prior its transition to detonation. *Aerosp. Sci. Technol.* **106**, 106203.

CHENG, J., ZHANG, B., LIU, H. & WANG, F. 2021*a* The precursor shock wave and flame propagation enhancement by CO2 injection in a methane-oxygen mixture. *Fuel* **283**, 118917.

CHENG, J., ZHANG, B., NG, D.H., LIU, H. & WANG, F. 2021*b* Effects of inert gas jet on the transition from deflagration to detonation in a stoichiometric methane-oxygen mixture. *Fuel* **285**, 119237.

COOPER, M., JACKSON, S., AUSTIN, J., WINTENBERGER, E. & SHEPHERD, J. 2002 Direct experimental impulse measurements for detonations and deflagrations. *J. Propul. Power* **18** (5), 1033–1041.

DEITERDING, R. 2003 Parallel adaptive simulation of multi-dimensional detonation structures. PhD thesis, Brandenburgische Technische Universität Cottbus.

DEITERDING, R. 2011 Block-structured adaptive mesh refinement-theory, implementation and application. *Esaim: Proc.* **34**, 97–150.

ETTNER, F. 2013 Effiziente numerische Simulation des Deflagrations - Detonations - Übergangs. PhD thesis, Technische Universität München, München.

ETTNER, F., VOLLMER, K.G. & SATTELMAYER, T. 2013 Mach reflection in detonations propagating through a gas with a concentration gradient. *Shock Waves* **23** (3), 201–206.

FAN, J. & XIAO, H. 2022 Flame acceleration and transition to detonation in non-uniform hydrogen-air mixtures in an obstructed channel with different obstacle arrangements. *Fire Safety J.* **133**, 103660.

FANG, Y., HU, Z., TENG, H., JIANG, Z. & NG, H.D. 2017 Numerical study of inflow equivalence ratio inhomogeneity on oblique detonation formation in hydrogen–air mixtures. *Aerosp. Sci. Technol.* **71**, 256–263.

FICKETT, W. & DAVIS, W.C. 2000 *Detonation: Theory and Experiment*. Courier Corporation.

FROLOV, S.M., SMETANYUK, V.A., AKSENOV, V.S. & KOVAL', A.S. 2017 Deflagration-to-detonation transition in crossed-flow fast jets of propellant components. *Dokl. Phys. Chem.* **476** (1), 153–156.

GAMEZO, V.N., BACHMAN, C.L. & ORAN, E.S. 2021 Flame acceleration and DDT in large-scale obstructed channels filled with methane-air mixtures. *Proc. Combust. Inst.* **38** (3), 3521–3528.

GAMEZO, V.N., DESBORDES, D. & ORAN, E.S. 1999 Formation and evolution of two-dimensional cellular detonations. *Combust. Flame* **116** (1–2), 154–165.

GAMEZO, V.N., OGAWA, T. & ORAN, E.S. 2007 Numerical simulations of flame propagation and DDT in obstructed channels filled with hydrogen–air mixture. *Proc. Combust. Inst.* **31** (2), 2463–2471.

GAMEZO, V.N., OGAWA, T. & ORAN, E.S. 2008 Flame acceleration and DDT in channels with obstacles: effect of obstacle spacing. *Combust. Flame* **155**, 302–315.

GOODWIN, D.G., MOFFAT, H.K. & SPETH, R.L. 2009 Cantera: an object-oriented software toolkit for chemical kinetics, thermodynamics, and transport processes. Caltech.

GOODWIN, G.B., HOUIM, R.W. & ORAN, E.S. 2016 Effect of decreasing blockage ratio on DDT in small channels with obstacles. *Combust. Flame* **173**, 16–26.

GROGAN, K.P. & IHME, M. 2015 Weak and strong ignition of hydrogen/oxygen mixtures in shock-tube systems. *Proc. Combust. Inst.* **35** (2), 2181–2189.

GROGAN, K.P. & IHME, M. 2017 Regimes describing shock boundary layer interaction and ignition in shock tubes. *Proc. Combust. Inst.* **36** (2), 2927–2935.

HAGHDOOST, M.R., EDGINGTON-MITCHELL, D., NADOLSKI, M., KLEIN, R. & OBERLEITHNER, K. 2020 Dynamic evolution of a transient supersonic trailing jet induced by a strong incident shock wave. *Phys. Rev. Fluids* **5** (7), 073401.

HAN, W., HUANG, J., GU, G., WANG, C. & LAW, C.K. 2020 Surface heat loss and chemical kinetic response in deflagration-to-detonation transition in microchannels. *Phys. Rev. Fluids* **5** (5), 053201.

HAN, W., WANG, C. & LAW, C.K. 2019 Role of transversal concentration gradient in detonation propagation. *J. Fluid Mech.* **865**, 602–649.

HU, X., ZHANG, D., KHOO, B.C. & JIANG, Z. 2005 The structure and evolution of a two-dimensional H2/O2/Ar cellular detonation. *Shock Waves* **14** (1), 37–44.

ISHII, K. & KOJIMA, M. 2007 Behavior of detonation propagation in mixtures with concentration gradients. *Shock Waves* **17** (1–2), 95–102.

IVANOV, M.F., KIVERIN, A.D. & LIBERMAN, M.A. 2011 Hydrogen-oxygen flame acceleration and transition to detonation in channels with no-slip walls for a detailed chemical reaction model. *Phys. Rev.* E *Stat. Nonlinear* **83** (5), 056313.

IWATA, K., IMAMURA, O., AKIHAMA, K., YAMASAKI, H., NAKAYA, S. & TSUE, M. 2021 Numerical study of self-sustained oblique detonation in a non-uniform mixture. *Proc. Combust. Inst.* **38** (3), 3651–3659.

IWATA, K., NAKAYA, S. & TSUE, M. 2017 Wedge-stabilized oblique detonation in an inhomogeneous hydrogen–air mixture. *Proc. Combust. Inst.* **36** (2), 2761–2769.

JACHIMOWSKI, C.J. 1988 An analytical study of the hydrogen-air reaction mechanism with application to scramjet combustion. *No*. L-16372.

JIANG, C., PAN, J., WENG, J., LI, J. & QUAYE, E.K. 2022*a* Role of concentration gradient in the re-initiation of H2/O2 detonation in a 90° bifurcated channel. *Aerosp. Sci. Technol.* **120**, 107281.

JIANG, C., PAN, J., ZHU, Y., LI, J., CHEN, H. & QUAYE, E.K. 2022*b* Influence of concentration gradient on detonation re-initiation in a bifurcated channel. *Fuel* **307**, 121895.

KAPS, P. & RENTROP, P. 1979 Generalized Runge-Kutta methods of order four with stepsize control for stiff ordinary differential equations. *Numer. Math.* **33** (1), 55–68.

KESSLER, D.A., GAMEZO, V.N. & ORAN, E.S. 2010 Simulations of flame acceleration and deflagration-to-detonation transitions in methane-air systems. *Combust. Flame* **157**, 2063–2077.

KESSLER, D.A., GAMEZO, V.N. & ORAN, E.S. 2011 Detonation propagation through a gradient in fuel composition. In Paper presented at the *Proceedings of the 23th International Colloquium on the Dynamics of Explosions and Reacting Systems, Irvine, CA*.

KESSLER, D.A., GAMEZO, V.N. & ORAN, E.S. 2012 Gas-phase detonation propagation in mixture composition gradients. *Phil. Trans. R. Soc.* A*: Math. Phys. Engng Sci.* **370** (1960), 567–596.

KNOX, B., FORLITI, D., STEVENS, C., HOKE, J. & SCHAUER, F. 2011 A comparison of fluidic and physical obstacles for deflagration-to-detonation transition. In *49th AIAA Aerospace Sciences Meeting Including the New Horizons Forum and Aerospace Exposition*, 587.

KUZNETSOV, M.S., ALEKSEEV, V.I., DOROFEEV, S.B., MATSUKOV, I.D. & BOCCIO, J.L. 1998 Detonation propagation, decay, and reinitiation in nonuniform gaseous mixtures. *Symp. (Intl) Combust.* **27** (2), 2241–2247.

LAW, C.K. 2010 *Combustion Physics*. Cambridge University Press.

LEE, J., KNYSTAUTAS, R. & YOSHIKAWA, N. 1980 Photochemical initiation of gaseous detonations. In *Gas Dynamics of Explosions and Reactive Systems*, pp. 971–982. Elsevier.

LEHR, H.F. 1972 Experiments on shock-induced combustion. *Astr. Acta* **17**, 589–597.

LI, T., WANG, X., XU, B. & KONG, F. 2021 An efficient approach to achieve flame acceleration and transition to detonation. *Phys. Fluids* **33** (5), 056103.

LI, X. & ZHANG, Q. 1997 A comparative numerical study of the Richtmyer-Meshkov instability with nonlinear analysis in two and three dimensions. *Phys. Fluids* **9**, 3069–3077.

LUAN, Z., HUANG, Y., GAO, S. & YOU, Y. 2022 Formation of multiple detonation waves in rotating detonation engines with inhomogeneous methane/oxygen mixtures under different equivalence ratios. *Combust. Flame* **241**, 112091.

MAHMOUDI, Y., KARIMI, N., DEITERDING, R. & EMAMI, S. 2014 Hydrodynamic instabilities in gaseous detonations: comparison of Euler, Navier–Stokes, and large-eddy simulation. *J. Propul. Power* **30** (2), 384–396.

MAHMOUDI, Y. & MAZAHERI, K. 2011 High resolution numerical simulation of the structure of 2-D gaseous detonations. *Proc. Combust. Inst.* **33** (2), 2187–2194.

MAHMOUDI, Y. & MAZAHERI, K. 2015 High resolution numerical simulation of triple point collision and origin of unburned gas pockets in turbulent detonations. *Acta Astronaut.* **115**, 40–51.

MATHUR, S., TONDON, P. & SAXENA, S. 1967 Thermal conductivity of binary, ternary and quaternary mixtures of rare gases. *Mol. Phys.* **12** (6), 569–579.

MCGARRY, J.P. & AHMED, K.A. 2017 Flame–turbulence interaction of laminar premixed deflagrated flames. *Combust. Flame* **176**, 439–450.

METROW, C., GRAY, S. & CICCARELLI, G. 2021 Detonation propagation through a nonuniform layer of hydrogen-oxygen in a narrow channel. *Intl J. Hydrogen Energy* **46** (41), 21726–21738.

MI, X., HIGGINS, A., NG, H.D., KIYANDA, C. & NIKIFORAKIS, N. 2017 Propagation of gaseous detonation waves in a spatially inhomogeneous reactive medium. *Phys. Rev. Fluids* **2** (5), 053201.

NG, H.D., JU, Y. & LEE, J.H. 2007 Assessment of detonation hazards in high-pressure hydrogen storage from chemical sensitivity analysis. *Intl J. Hydrogen Energy* **32** (1), 93–99.

OGAWA, T., GAMEZO, V.N. & ORAN, E.S. 2013 Flame acceleration and transition to detonation in an array of square obstacles. *J. Loss Prev. Process Ind.* **26** (2), 355–362.

ORAN, E.S., CHAMBERLAIN, G. & PEKALSKI, A. 2020 Mechanisms and occurrence of detonations in vapor cloud explosions. *Prog. Energy Combust. Sci.* **77**, 100804.

ORAN, E.S., JONES, D.A. & SICHEL, M. 1992 Numerical simulations of detonation transmission. *Proc. R. Soc. Lond. Ser.* A*: Math. Phys. Sci.* **436** (1897), 267–297.

PENG, H., HUANG, Y., DEITERDING, R., LUAN, Z., XING, F. & YOU, Y. 2018 Effects of jet in crossflow on flame acceleration and deflagration to detonation transition in methane–oxygen mixture. *Combust. Flame* **198**, 69–80.

PENG, H., HUANG, Y., DEITERDING, R., YOU, Y. & LUAN, Z. 2019 Effects of transverse jet parameters on flame propagation and detonation transition in hydrogen–oxygen–argon mixture. *Combust. Sci. Technol.* **00**, 1–22.

RADULESCU, M.I., SHARPE, G.J., LAW, C.K. & LEE, J.H. 2007 The hydrodynamic structure of unstable cellular detonations. *J. Fluid Mech.* **580**, 31–81.

RADULESCU, M.I., SHARPE, G.J., LEE, J., KIYANDA, C., HIGGINS, A. & HANSON, R. 2005 The ignition mechanism in irregular structure gaseous detonations. *Proc. Combust. Inst.* **30** (2), 1859–1867.

ROY, G.D., FROLOV, S.M., BORISOV, A.A. & NETZER, D.W. 2004 Pulse detonation propulsion: challenges, current status, and future perspective. *Prog. Energy Combust. Sci.* **30** (6), 545–672.

SAEID, M.H.S., KHADEM, J. & EMAMI, S. 2021 Numerical investigation of the mechanism behind the deflagration to detonation transition in homogeneous and inhomogeneous mixtures of H2-air in an obstructed channel. *Intl J. Hydrogen Energy* **46** (41), 21657–21671.

SAEID, M.H.S., KHADEM, J., EMAMI, S. & GHODRAT, M. 2022 Effect of diffusion time on the mechanism of deflagration to detonation transition in an inhomogeneous mixture of hydrogen-air. *Intl J. Hydrogen Energy* **47** (55), 23411–23426.

SHARPE, G.J. 2001 Transverse waves in numerical simulations of cellular detonations. *J. Fluid Mech.* **447**, 31–51.

SOCHET, I., LAMY, T. & BROSSARD, J. 2000 Experimental investigation on the detonability of non-uniform gaseous mixtures. *Shock Waves* **10** (5), 363–376.

SONG, Q., HAN, Y. & CAO, W. 2020 Numerical investigation of self-sustaining modes of 2D planar detonations under concentration gradients in hydrogen–oxygen mixtures. *Intl J. Hydrogen Energy* **45** (53), 29606–29615.

SUBBOTIN, V. 1975 Two kinds of transverse wave structures in multifront detonation. *Combust. Explos. Shock Waves* **11** (1), 83–88.

SUN, X. & LU, S. 2020 On the mechanisms of flame propagation in methane-air mixtures with concentration gradient. *Energy* **202**, 117782.

TANG-YUK, K.C., MI, X., LEE, J.H.S., NG, H.D. & DEITERDING, R. 2022 Transmission of a detonation wave across an inert layer. *Combust. Flame* **236**, 111769.

TARRANT, D.J., CHAMBERS, J.M., JOO, P.H. & AHMED, K. 2020 Influence of transverse slot jet on premixed flame acceleration. *J. Propul. Power* **36**, 59–67.

THOMAS, G.O., SUTTON, P. & EDWARDS, D.H. 1991 The behavior of detonation waves at concentration gradients. *Combust. Flame* **84** (3–4), 312–322.

VOLLMER, K., ETTNER, F. & SATTELMAYER, T. 2012 Deflagration-to-detonation transition in hydrogen-air mixtures with a concentration gradient. *Combust. Sci. Technol.* **184** (10–11), 1903–1905.

WANG, C.J. & WEN, J.X. 2017 Numerical simulation of flame acceleration and deflagration-to-detonation transition in hydrogen-air mixtures with concentration gradients. *Intl J. Hydrogen Energy* **42** (11), 7657–7663.

WANG, Y., HUANG, C., DEITERDING, R., CHEN, H. & CHEN, Z. 2020 Propagation of gaseous detonation across inert layers. *Proc. Combust. Inst.* **38**, 3555–3563.

XIAO, H. & ORAN, E.S. 2019 Shock focusing and detonation initiation at a flame front. *Combust. Flame* **203**, 397–406.

XIAO, H. & ORAN, E.S. 2020 Flame acceleration and deflagration-to-detonation transition in hydrogen-air mixture in a channel with an array of obstacles of different shapes. *Combust. Flame* **220**, 378–393.

YAO, K., YANG, P., TENG, H., CHEN, Z. & WANG, C. 2022 Effects of injection parameters on propagation patterns of hydrogen-fueled rotating detonation waves. *Intl J. Hydrogen Energy* **47** (91), 38811–38822.

YHUEL, E., RIBERT, G. & DOMINGO, P. 2023 Numerical simulation of laminar premixed hydrogen-air flame/shock interaction in semi-closed channel. *Proc. Combust. Inst.* **39** (3), 3021–3029.

YUAN, X., ZHOU, J., MI, X. & NG, H.D. 2019 Numerical study of cellular detonation wave reflection over a cylindrical concave wedge. *Combust. Flame* **202**, 179–194.

ZEL'DOVICH, Y.B., LIBROVICH, V.B., MAKHVILADZE, G.M. & SIVASHINSKY, G.I. 1970 On the development of detonation in a non-uniformly preheated gas. *Astronaut. Acta* **15** (5), 313–321.

ZHANG, L., QIAO, H., LIANG, J., WANG, Y., DING, M., YANG, L. & SUN, M. 2024 Experimental study of scramjet cavity with rear edge slots and its performance in combustion enhancement. *Acta Mechanica Sin.* **40** (1), 323135.

ZHAO, W., DEITERDING, R., LIANG, J., CAI, X. & WANG, X. 2023*a* Detonation simulations in supersonic flow under circumstances of injection and mixing. *Proc. Combust. Inst.* **39** (3), 2895–2903.

ZHAO, W., DEITERDING, R., LIANG, J., WANG, X., CAI, X. & DUELL, J. 2023*b* Adaptive simulations of flame acceleration and detonation transition in subsonic and supersonic mixtures. *Aerosp. Sci. Technol.* **136**, 108205.

ZHAO, W., FAN, C., DEITERDING, R., LI, X., LIANG, J. & YANG, X. 2024 A new rapid deflagration-to-detonation transition in a short smooth tube. *Phys. Fluids* **36** (3), 036104.

ZHAO, W., LIANG, J., DEITERDING, R., CAI, X. & WANG, X. 2021 Effect of transverse jet position on flame propagation regime. *Phys. Fluids* **33** (9), 091704.

ZHAO, W., LIANG, J., DEITERDING, R., CAI, X. & WANG, X. 2022*a* Flame–turbulence interactions during flame acceleration using solid and fluid obstacles. *Phys. Fluids* **34** (10), 106106.

ZHAO, X., WANG, J., GAO, L., WANG, X. & ZHU, Y. 2022*b* Flame acceleration and onset of detonation in inhomogeneous mixture of hydrogen-air in an obstructed channel. *Aerosp. Sci. Technol.* **130**, 107944.

ZHENG, W., KAPLAN, C.R., HOUIM, R.W. & ORAN, E.S. 2019 Flame acceleration and transition to detonation: effects of a composition gradient in a mixture of methane and air. *Proc. Combust. Inst.* **37** (3), 3521–3528.